

Designing Broadband Pulsed Dynamic Nuclear Polarization Sequences in Static Solids

Nino Wili,^{1, a)} Anders Bodholt Nielsen,² Laura Alicia Völker,¹ Lukas Schreder,¹ Niels Chr. Nielsen,² Gunnar Jeschke,¹ and Kong Ooi Tan^{3, b)}

¹⁾ *Department of Chemistry and Applied Biosciences, Laboratory of Physical Chemistry, ETH Zurich, Vladimir-Prelog-Weg 2, 8093 Zurich, Switzerland*

²⁾ *Interdisciplinary Nanoscience Center (iNANO) and Department of Chemistry, Aarhus University, Gustav Wieds Vej 14, DK-8000 Aarhus C, Denmark*

³⁾ *Laboratoire des Biomolécules, LBM, Département de Chimie, École Normale Supérieure, PSL University, Sorbonne Université, CNRS, 75005 Paris, France*

(Dated: 15 March 2022)

Dynamic nuclear polarization (DNP) is an NMR hyperpolarization technique that mediates polarization transfer from highly polarized unpaired electrons to NMR-active nuclei via microwave (mw) irradiation. The ability to generate arbitrarily shaped mw pulses using arbitrary waveform generators opens up the opportunity to remarkably improve the robustness and versatility of DNP, in many ways resembling the early stages of pulsed NMR. We present here novel design principles based on single-spin vector effective Hamiltonian theory to develop new broadband DNP pulse sequences, namely an adiabatic XiX-DNP experiment and a broadband amplitude modulated signal enhanced (BASE) experiment. We demonstrate that the adiabatic BASE pulse sequence may achieve a DNP ¹H enhancement factor of ~ 360 , a record that outperforms all previously known pulsed DNP sequences at ~ 0.35 T and 80 K in static solids. The bandwidth of the BASE-DNP experiments is about 3 times the ¹H Larmor frequency (~ 50 MHz).

I. INTRODUCTION

Dynamic nuclear polarization (DNP) is a powerful tool to increase the sensitivity of nuclear magnetic resonance (NMR) by transferring the much higher polarization of electron spins to nuclear spins with a theoretical maximum enhancement factor $\varepsilon \sim 658^{1,2}$ for ¹H. The hyperpolarization method allows one to study systems that suffer from poor NMR sensitivity with reduced measurement time or cost. For instance, a DNP experiment with $\varepsilon \sim 100$ performed in one hour would have taken ~ 1 year without mw irradiation for the same-quality spectrum. This opens up the possibility to extract important structural information from small molecules, biological samples, or inorganic materials that are otherwise inaccessible due to poor NMR sensitivity.

Since the discovery of DNP in the fifties³ tremendous progress has been made, and there are two main DNP methods: dissolution DNP⁴ and *in situ* solid-state DNP NMR potentially combined with magic-angle spinning (MAS)⁵. The former category typically polarizes a static sample at low temperatures (< 2 K) and moderate magnetic fields (3.4-10.1 T)⁶, where the electron polarization approaches unity. Following that, the sample undergoes a dissolution process prior to be transported to a high-resolution NMR magnet or MRI system for detection in solution state. The *in situ* static sample or MAS DNP NMR approach performs the hyperpolarization and NMR detection process on solid samples in the same high-resolution magnet typically at temperatures

below 100 K. To facilitate efficient DNP processes at these relatively higher temperatures and fields, it is necessary to use high-power mw sources known as gyrotrons. Although these DNP methods have successfully enabled many biological molecules and materials to be studied with superior sensitivity^{2,7}, it is noted that the DNP efficiency deteriorates at higher magnetic fields⁸. Despite new classes of biradicals that have been reported to circumvent this issue^{9,10}, the DNP performance is sample-dependent and varies with rotor sizes (or mw penetration). Hence, it would be highly desirable to develop a general DNP method with a consistent performance across different magnetic fields, paramagnetic polarizing agents, and other experimental conditions. One of the major reasons that hinders the development towards this goal is that most contemporary DNP approaches use continuous-wave (CW) mw irradiation, where the amplitude, phase, and frequency cannot be easily controlled. As a consequence only four main CW-DNP mechanisms have been discovered so far, namely: Overhauser effect (OE)³, the solid effect (SE)^{11,12}, the cross effect (CE)^{13,14}, and thermal mixing (TM)^{15,16}. In comparison, hundreds of NMR pulse sequences have been invented to date, for purposes ranging from polarization transfer, distance measurement, to determination of dynamics and chemical environments, etc. An important aspect in choosing the right pulse sequence is the bandwidth, an issue relatively less discussed in DNP. The EPR line widths of many radicals are often broad, especially at high fields due to large *g*-anisotropy. The linewidth of a typical nitroxide radical is ~ 1 GHz at 9.4 T,¹⁷ which is orders of magnitude higher than the electron Rabi fields conferred by the currently available mw power. The aim of this study is to demonstrate - albeit at lower field - ways

^{a)} Electronic mail: nino.wili@alumni.ethz.ch

^{b)} Electronic mail: kong-ooi.tan@ens.psl.eu

to design broadband and efficient DNP techniques exploiting shaped pulses generated by arbitrary waveform generators (AWG) at different mw power conditions.

Our approach to the design of broadband pulsed DNP experiments has been inspired by previous pulsed DNP techniques, namely nuclear orientation via spin locking (NOVEL)^{18–20}, ramped-amplitude (RA)-NOVEL²¹, off-resonance NOVEL²², the integrated solid effect (ISE)^{23,24}, the adiabatic solid effect (ASE)²⁵, nuclear rotating frame (NRF)-DNP²⁶, the dressed spin solid effect (DSSE)²⁷, PulsePol²⁸, and time-optimized pulsed (TOP)-DNP²⁹. Among these sequences, we would like to emphasize that the TOP-DNP sequence is substantially different from others, i.e., the initial truncation of the electron-nuclear dipolar couplings by the nuclear Zeeman term can be reintroduced by mw irradiation to transfer polarization in DNP. The methods to reintroduce these couplings are mathematically similar to and inspired by the dipolar recoupling techniques in MAS solid-state NMR spectroscopy, where rf irradiation interferes with the rotational averaging of dipolar couplings. Following this, a phase-alternating low-power X-inverse X (XiX)-DNP has been demonstrated recently using similar average Hamiltonian and operator-based Floquet theory design principles³⁰. In this work, we further introduce an alternative design strategy based on single-spin vector effective Hamiltonian theory^{31,32}, which incorporates Fourier coefficients (exploited in Floquet theory) into average Hamiltonian theory. This theoretical framework is applicable to *any* arbitrary periodic DNP experiments, and will here be used for designing broadband DNP experiments. We will examine these sequences by numerical simulations and experiments at 0.35 T/ 9.8 GHz/ 15 MHz on OX063 trityl radicals doped in a glycerol-water mixture at 80 K.

II. THEORY

We will describe the overall Hamiltonian for an electron-nuclear spin system followed by a series of transformations leading to a convergent effective Hamiltonian. The Hamiltonian is cast as a Fourier expansion, which allows us to identify the resonance conditions and determine the effective couplings that govern the DNP polarization transfer. The procedure takes inspiration from previous single-vector effective Hamiltonian approaches described recently in relation to solid-state NMR dipolar recoupling³¹ and liquid-state NMR isotropic mixing³².

While the theory outlined in the following is valid and extendable to describe systems with multiple electrons and nuclei, we will for simplicity stick to a two-spin system comprised of one electron spin (S) and one nuclear spin (I). The laboratory-frame Hamiltonian is given by

$$\mathcal{H} = \omega_S S_z + \mathcal{H}_{\text{mw}} + \vec{S} \cdot \mathbf{A} \cdot \vec{I} + \omega_I I_z \quad , \quad (1)$$

with $\omega_S = -\gamma_e B_0$ and $\omega_I = -\gamma_n B_0$ being angular frequencies for the electron and nuclear Zeeman interac-

tions, respectively (for an e-¹H system $\omega_S > 0$ and $\omega_I < 0$). γ , \mathbf{A} , \mathcal{H}_{mw} , and B_0 refer to the gyromagnetic ratio, the hyperfine coupling tensor, the Hamiltonian of the mw irradiation, and the external static magnetic field along the z -axis, respectively. Upon transformation to the electron rotating frame and employing the high-field approximation, the first-order effective Hamiltonian becomes

$$\tilde{\mathcal{H}} = \underbrace{\Omega_S S_z + \tilde{\mathcal{H}}_{\text{mw}}}_{\mathcal{H}_{\text{control}}} + \underbrace{A_{zz} S_z I_z + B S_z I_x + \omega_I I_z}_{\mathcal{H}'} \quad , \quad (2)$$

where $\Omega_S = \omega_S - \omega_{\text{mw}}$ is the mw offset frequency; A_{zz} and $B = \sqrt{A_{zx}^2 + A_{zy}^2}$ are the secular and pseudosecular coupling, respectively. Note that the B term originates purely from the dipolar coupling, which is averaged to zero in solution state. We will restrict our discussions to spin systems in the regime where $|A_{zz}|, |B| \ll |\omega_I|$, so that the effect of the spin diffusion barrier can be neglected in this context, i.e. the electron-nuclear distance falls in the range of 4–10 Å^{33–36}.

We now move into the interaction frame with the control field $\mathcal{H}_{\text{control}}$, which contains all explicit information (amplitudes, frequencies, and phases) about mw pulses:

$$\begin{aligned} \tilde{\mathcal{H}}' &= U_{\text{control}}^\dagger \mathcal{H}' U_{\text{control}} \\ &= \sum_{\chi=x,y,z} R_{\chi z}^{(\text{control})}(t) S_\chi (A_{zz} I_z + B I_x) + \omega_I I_z \quad , \end{aligned} \quad (3)$$

where $U_{\text{control}}(t) = \hat{T} \exp(-i \int_0^t \mathcal{H}_{\text{control}}(\tau) d\tau)$ and \hat{T} is the Dyson time-ordering operator. The time-dependent rotation matrix $R_{\chi z}^{(\text{control})}$ represents the interaction-frame trajectory of the electron spin under the mw pulse sequence. Then, we can calculate an effective time-independent Hamiltonian using standard average Hamiltonian theory, provided $\mathcal{H}_{\text{control}}(t)$ is periodic over a given period $\tau_m = 2\pi/\omega_m$ (where ω_m is the modulation frequency of the pulse sequence), i.e., $\mathcal{H}_{\text{control}}(t) = \mathcal{H}_{\text{control}}(t + \tau_m)$. We note that a periodic Hamiltonian does not necessarily need to have an identity propagator over one cycle.

Although the control propagator U_{control} , which is equivalent to $R_{\chi z}^{(\text{control})}$, may not necessarily be cyclic in the normal mw rotating frame, it is always possible to find a frame in which the new transformed control propagator becomes cyclic. Having a cyclic propagator is particularly useful in both characterizing and gaining useful insight into the pulse sequence. It is also a prerequisite for the application of average Hamiltonian theory to the interaction frame Hamiltonian. Hence, we choose a frame with its z -axis aligned with the effective field (ω_{eff})^{31,32}, whose magnitude and direction can be determined using quaternion algebra^{37–39}. We indicate this frame in the following with a tilde on the \tilde{S} -spin operators. This leads to

$$\tilde{\mathcal{H}}' = \sum_{\chi=x,y,z} R_{\chi z}^{(\text{eff})}(t) \tilde{S}_\chi (A_{zz} I_z + B I_x) - \omega_{\text{eff}}^{(S)} \tilde{S}_z + \omega_I I_z \quad (4)$$

with

$$\begin{aligned} R_{\chi z}^{(\text{eff})}(t) &= [R_z(-\omega_{\text{eff}}^{(S)}t) \cdot R^{(\text{flip})}(\beta) \cdot R^{(\text{control})}]_{\chi z}(t) \\ &= \sum_{k=-\infty}^{\infty} a_{\chi z}^{(k)} e^{ik\omega_m t} \end{aligned} \quad (5)$$

representing a three-step transformation comprised of (1) go into the control frame; (2) flip the coordinate system by β so that it is aligned with $\omega_{\text{eff}}^{(S)}\tilde{S}_z$; (3) rotate the frame by an angle $\omega_{\text{eff}}^{(S)}t$ around the new z axis.^{31,32} Moreover, Eq. (5) is cyclic, i.e., $[R_{\chi z}^{(\text{eff})}(t+\tau_m)]_{\chi z} = R_{\chi z}^{(\text{eff})}(t)$, and the elements of the overall rotation matrix may be expressed in terms of a Fourier series as given in the right-hand side of the equation. The term $-\omega_{\text{eff}}^{(S)}\tilde{S}_z$ incorporates the Coriolis term originating from step (3) above.

We transform the nuclear part (I) of the Hamiltonian into an interaction frame with closest match between the mw modulation frequency ω_m and ω_I to obtain the I -spin

effective field

$$\omega_{\text{eff}}^{(I)} = \omega_I - k_I \omega_m \text{ with } k_I = \text{round}\left(\frac{\omega_I}{\omega_m}\right), \quad (6)$$

which is then used to form the propagator $U_{\text{eff}} = \exp(-ik_I \omega_m t I_z)$ that transforms $\tilde{\mathcal{H}}'$ (Eq. (4)) into

$$\begin{aligned} \tilde{\mathcal{H}}' &= U_{\text{eff}}^\dagger \tilde{\mathcal{H}} U_{\text{eff}} - k_I \omega_m I_z \\ &= \sum_{\chi=x,y,z} \sum_{k=-\infty}^{\infty} a_{\chi z}^{(k)} e^{ik\omega_m t} \tilde{S}_\chi \times \\ &\quad \left(A_{zz} I_z + \frac{B}{2} (e^{ik_I \omega_m t} I^+ + e^{-ik_I \omega_m t} I^-) \right) \\ &\quad - \omega_{\text{eff}}^{(S)} \tilde{S}_z + \omega_{\text{eff}}^{(I)} I_z \quad . \end{aligned} \quad (7)$$

Next, we apply first-order average Hamiltonian theory (AHT) and recognize that index k in Eq. (7) has to be either $= \pm k_I$ or $= 0$. All other terms vanish upon integration over one modulation period, leading to

$$\begin{aligned} \tilde{\mathcal{H}}^{(1)} &= A_{zz} \sum_{\chi=x,y,z} a_{\chi z}^{(0)} \tilde{S}_\chi I_z + \frac{B}{2} \tilde{S}_z \left(a_{zz}^{(-k_I)} I^+ + a_{zz}^{(k_I)} I^- \right) \\ &\quad + \frac{B}{4} \left(a_{+z}^{(-k_I)} \tilde{S}^+ I^+ + a_{-z}^{(-k_I)} \tilde{S}^- I^+ + a_{+z}^{(k_I)} \tilde{S}^+ I^- + a_{-z}^{(k_I)} \tilde{S}^- I^- \right) - \omega_{\text{eff}}^{(S)} \tilde{S}_z + \omega_{\text{eff}}^{(I)} I_z \quad , \end{aligned} \quad (8)$$

where we define $a_{xz}^{(q)} \tilde{S}_x + a_{yz}^{(q)} \tilde{S}_y = \frac{1}{2}(a_{+z}^{(q)} \tilde{S}^+ + a_{-z}^{(q)} \tilde{S}^-)$ and $a_{\pm z}^{(q)} = a_{xz}^{(q)} \mp i a_{yz}^{(q)}$. Since the effective Hamiltonian must be Hermitian, it is enforced that $a_{-z}^{(q)} = \left(a_{+z}^{(-q)}\right)^*$.

A. Identifying resonance conditions and scaling factors

We note that the effective Hamiltonian $\tilde{\mathcal{H}}^{(1)}$ (Eq. (8)) was derived without explicitly describing the details of the pulse sequence, i.e., it has a general form and is applicable to *all* periodic EPR or DNP sequences acting on a two-spin electron-nucleus system in the regime where $|A_{zz}|, |B| \ll |\omega_I|$. This is possible because the details of these pulses sequences are implicitly encoded in the scaling factors $a_{\chi z}$ of the corresponding resonance conditions, which will be discussed in the following.

For polarization-transfer experiments, it is necessary to retain only either the zero- or double-quantum (ZQ or DQ) operators and suppress all other non-commuting operators. This is achieved by matching the effective fields $(-\omega_{\text{eff}}^{(S)}\tilde{S}_z, \omega_{\text{eff}}^{(I)}I_z)$ in Eq. (8), i.e., by finding the DNP matching conditions. One can identify a resonance condition $\omega_{\text{eff}}^{(S)} = -\omega_{\text{eff}}^{(I)}$, where only the ZQ operators ($\tilde{S}^\pm I^\mp$) survive because the DQ terms ($\tilde{S}^\pm I^\pm$) are truncated by the larger non-commuting $I_z + \tilde{S}_z$ term. Note

that a converse case is found in the other resonance condition, $\omega_{\text{eff}}^{(S)} = \omega_{\text{eff}}^{(I)}$, where only the DQ terms remain due to a similar truncation in the ZQ subspace. All other terms can be neglected as long as they are much smaller than the effective fields. This is a good approximation for weakly coupled protons involved in DNP, and will be checked by numerical simulations below. While the $A_{zz}\tilde{S}_z I_z$ term commutes with the effective fields, it shifts both energy levels in the same direction within the respective subspace (ZQ or DQ). Thus, the energy difference and resonance conditions remain unchanged. By neglecting the the terms discussed above, we obtain

$$\begin{aligned} \tilde{\mathcal{H}}^{(1)} &= \frac{B}{4} \left(a_{-z}^{(\mp k_I)} \tilde{S}^- I^\pm + a_{+z}^{(\pm k_I)} \tilde{S}^+ I^\mp \right) \\ &\quad - \omega_{\text{eff}}^{(S)} \tilde{S}_z + \omega_{\text{eff}}^{(I)} I_z \quad \text{for } \omega_{\text{eff}}^{(S)} \approx \mp \omega_{\text{eff}}^{(I)} \quad , \end{aligned} \quad (9)$$

and the $\rho_0 \rightarrow I_z$ transfer mediated by the effective Hamiltonian can be calculated by using $U = \exp(-i\tilde{\mathcal{H}}^{(1)}t)$:

$$\begin{aligned} \langle I_z \rangle(t) &= \frac{\gamma_e}{\gamma_n} \langle \rho_0 | \tilde{S}_z \rangle \text{Tr}\{U \tilde{S}_z U^\dagger I_z\} / \text{Tr}\{I_z^2\} \\ &= \pm \frac{\gamma_e}{\gamma_n} \langle \rho_0 | \tilde{S}_z \rangle \frac{B^2 a_{\mp}^2}{4\omega_{\mp}^2} \sin^2\left(\frac{1}{2}\omega_{\mp} t\right) \quad \text{for } \omega_{\text{eff}}^{(S)} \approx \mp \omega_{\text{eff}}^{(I)} \end{aligned} \quad (10)$$

with

$$a_{\mp} = \sqrt{a_{-z}^{(\mp k_I)} a_{+z}^{(\pm k_I)}} \quad (11)$$

representing a unitless scaling factor that dictates the transfer efficiency. The quantity

$$\omega_{\mp} = \sqrt{B^2 a_{\mp}^2 / 4 + (\Delta\omega_{\text{eff}}^{\mp})^2} \quad (12)$$

characterizes the DNP buildup rate, and it depends on the ‘‘mismatch’’ of the effective fields:

$$\Delta\omega_{\text{eff}}^{\mp}(\Omega_S) = \omega_{\text{eff}}^{(S)}(\Omega_S) \pm \omega_{\text{eff}}^{(I)} \quad , \quad (13)$$

where the mismatch can be electron offset-dependent $\Delta\omega_{\text{eff}}^{\mp}(\Omega_S)$. While the buildup is faster in case of a larger mismatch, the transfer amplitude is lower, similar to the situation of an off-resonance pulse in a two-level system. Note that the subscripts ‘-’ and ‘+’ in a_{\mp} and ω_{\mp} symbolize the ZQ and the DQ case, respectively. The prefactor $\frac{\gamma_e}{\gamma_n} \langle \rho_0 | \tilde{S}_z \rangle$ in Eq. (10) highlights that only the part of the electron density operator projected onto the effective field will be transferred to the nucleus via the ZQ/DQ operator.

The ZQ/DQ-operator-mediated transfers may be visualized by expressing the Hamiltonian (Eq. (9)) in terms of fictitious spin-1/2 operators^{40,41} $I_x^{\pm} = \frac{1}{2}(\tilde{S}^+ I^{\pm} + \tilde{S}^- I^{\mp})$, $I_y^{\pm} = \frac{1}{2i}(\tilde{S}^+ I^{\pm} - \tilde{S}^- I^{\mp})$, and $I_z^{\pm} = \frac{1}{2}(\tilde{S}_z \pm I_z)$. This results in

$$\begin{aligned} \tilde{\mathcal{H}}^{(1)} = & \frac{B}{2} \left(\text{Re}(a_{-z}^{(\mp k_I)}) I_x^{\mp} \mp \text{Im}(a_{-z}^{(\mp k_I)}) I_y^{\mp} \right) \\ & + \Delta\omega_{\text{eff}}^{-} I_z^{-} + \Delta\omega_{\text{eff}}^{+} I_z^{+} \quad , \quad (14) \end{aligned}$$

recalling the superscript signs - and + relate to ZQ and DQ operators, respectively. Figure 1 shows the evolution of spin operators in a diabatic (‘sudden’) (Fig. 1a) or adiabatic (Fig. 1b) manner in the ZQ/DQ subspace. At the exact resonance condition (mismatch $\Delta\omega_{\text{eff}}^{\mp} = 0$), the polarization-transfer expression simplifies to

$$\langle I_z \rangle(t) = \pm \frac{\gamma_e}{\gamma_n} \langle \rho_0 | \tilde{S}_z \rangle \sin^2 \left(\frac{B}{4} a_{\mp} t \right) \quad \text{for } \omega_{\text{eff}}^{(S)} = \mp \omega_{\text{eff}}^{(I)} \quad , \quad (15)$$

whose initial polarization buildup (small t) can be approximated by a Taylor series as

$$\langle I_z \rangle(t) \approx \pm \frac{\gamma_e}{\gamma_n} \langle \rho_0 | \tilde{S}_z \rangle \frac{B^2}{16} a_{\mp}^2 t^2 + \mathcal{O}(t^4) \quad \text{for } \omega_{\text{eff}}^{(S)} = \mp \omega_{\text{eff}}^{(I)} \quad . \quad (16)$$

We define the transfer parameter

$$f_{\mp} = \langle \rho_0 | \tilde{S}_z \rangle a_{\mp} \quad , \quad (17)$$

which allows us to semi-quantitatively evaluate the performance of a pulse sequence, before performing a detailed analysis by defining a particular spin system.

Finally, we should be aware that the choice of the effective field is not unique, and it requires a convention.

We choose $|\omega_{\text{eff}}^{(S)}|, |\omega_{\text{eff}}^{(I)}| \leq \omega_m/2$, which is an arbitrary but convenient decision. If we would allow for a larger effective field, it would become harder to keep track of resonance conditions. For our choice, there is one special case, when $|\omega_{\text{eff}}^{(I)}| \approx |\omega_{\text{eff}}^{(S)}| \approx |\omega_m|/2$. In this case, the ZQ and DQ resonance conditions are approximately fulfilled at the same time, because the difference or sum of the effective field matches the modulation frequency implying that a single scaling factor is not sufficient to describe the spin dynamics.

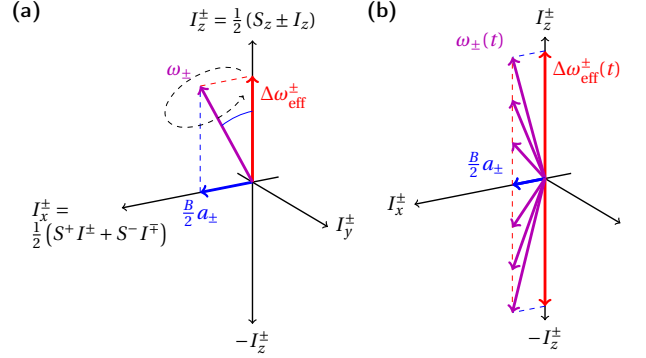


FIG. 1. Diagram of the effective (fictitious) spin-1/2 subspaces involved in DNP, with the - and + signs on operators and frequencies representing ZQ and DQ transfers, respectively. (a) A diabatic (‘sudden’) sequence with a constant mismatch. (b) Adiabatic sequence with slowly changing mismatch of the nuclear and electron effective fields. The effective ‘mismatch’ field is slowly dragged from +z to -z, corresponding to full polarization transfer. Note that a_{\mp} is not necessarily a constant. In principle there can also be terms proportional to I_y^{\pm} , which we ignored for the illustration.

B. Illustration of the interaction frame transformation

A central element in calculating the scaling factors a_{\mp} is the interaction frame transformations involved in Eqs. (3) - (5). Here, we give a concrete example of the elements of $R^{(\text{control})}$ and $R^{(\text{eff})}$ and their relationship. We consider an XiX-DNP experiment (parameters here not chosen to represent any good DNP sequence, but for easier explanation) with $\nu_1 = 4$ MHz, $t_{p,1} = 14$ ns, $t_{p,2} = 28$ ns, and $\Omega_S/2\pi = 25$ MHz (see Figure 3 for the pulse sequence description). Figure 2(a) shows the elements of the initial interaction frame transformation $R^{(\text{control})}(t)$ plotted over one period τ_m . The blue curves denote the trajectory of the normal rotating frame operator S_z . Note that $R^{(\text{control})}(0) = \mathbb{1} \neq R^{(\text{control})}(\tau_m)$, i.e. the trajectory is not cyclic with τ_m . This prohibits the straightforward application of average Hamiltonian theory and is the reason for the subsequent transformations. Figure 2(b) shows the three-dimensional trajectory of the original S_z operator in the initial interaction frame (the three blue components in panel (a)). The trajectory of

the first modulation period is marked in red. The end points of the subsequent five periods are shown as black dots in panel (b). The overall rotation from one period to the next can be described by an effective field shown in gray. This can be understood as a constant effective field, which can be removed by flipping the frame such that the effective field is along z , and then going into an interaction frame with said effective field. The result of this transformation, $R^{(\text{eff})}$, is shown in Figure 2(c). The z -axis in this new frame points along the effective field in Figure 2(b), and the effect of the overall rotation was eliminated by a counter rotation, i.e. start and end points of the trajectories are now the same. In Figure 2(c), all the coefficients are cyclic with time τ_m . A Fourier transform of the respective time-dependent coefficients directly yields $a_{\chi z}^{(k)}$ in Equation (5). An example

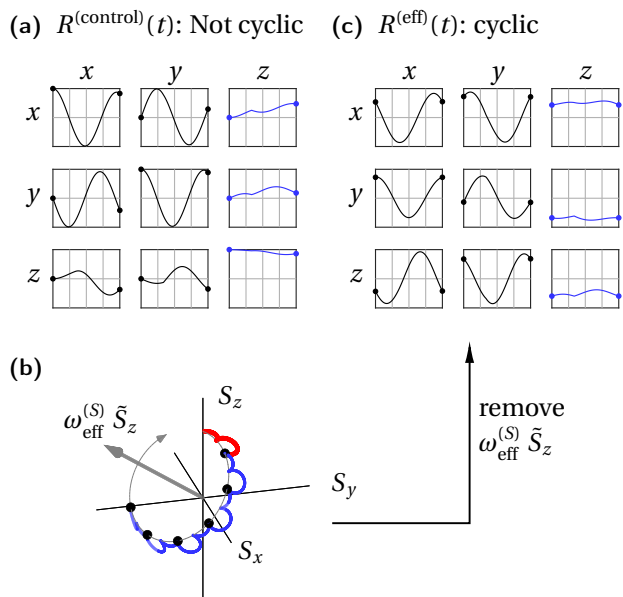


FIG. 2. Illustration for the interaction frames employed in this work, on the example of XiX-DNP (details in main text). (a) Illustration of the initial interaction frame transformation $R^{(\text{control})}(t)$. The individual plots show the evolution of rotation matrix elements over one period τ_m . (b) Three-dimensional trajectory of the original S_z operator in the initial interaction frame (the three blue components in (a)). The trajectory of the first modulation period is marked in red. The end points of the subsequent five periods are shown as black dots. The effective field describes the overall rotation of the sequence. (c) The same trajectory as in (a), but in the flipped, effective (or cyclic) frame. The start and end points are the same.

script to perform these calculations in MATLAB is given in the SI.

C. Adiabatic sweeps

It is advantageous to sweep the effective fields across the resonance conditions because it can improve the bandwidth and overall robustness of pulse sequences. Hence, we will address the effect of adiabatic sweeps through a resonance condition using the theoretical framework developed in this manuscript. For simplicity, we assume (1) only one resonance condition is swept during the experiment; (2) the changes in the scaling factors and the electron spin component along the effective field are sufficiently slow relative to the change in the effective fields, i.e., an adiabatic process.

To adiabatically invert the fictitious operator $I_z^\mp \rightarrow -I_z^\mp$ in the respective ZQ/DQ subspace (Eq. (14)), an adiabatic sweep is implemented by varying the offset (or resonance mismatch) in the ZQ/DQ subspace starting from large positive values ($\Delta\omega_{\text{eff}}^\mp \gg 0$), then slowly through zero ($\Delta\omega_{\text{eff}}^\mp = 0$), and then continue to large negative values ($\Delta\omega_{\text{eff}}^\mp \ll 0$). Note that the offset term in the ZQ/DQ subspace is usually not equivalent to the electron offset Ω_S . For instance, in the adiabatic NOVEL DNP sequence, the offset in the ZQ/DQ subspace is determined by the mismatched Rabi field $\omega_{1S}(t)$, although the electron offset is $\Omega_S = 0$ throughout the sequence. Figure 1(b) shows the schematic diagram of the described adiabatic sweep, which resulted in the spin evolution of $I_z^\mp \rightarrow I_z^\pm$ (in a subspace), which is mathematically equivalent to a $\tilde{S}_z \rightarrow I_z$ transfer.

To ensure that the sequence is adiabatic, one can calculate the adiabaticity Q_{crit} at the moment the resonance condition is passed^{42,43}

$$Q_{\text{crit}}^\mp = \frac{1}{4} \frac{(Ba_\mp)^2}{\frac{d}{dt} \Delta\omega_{\text{eff}}^\mp(t)} \quad (18)$$

which can be exploited to evaluate the polarization-transfer efficiency using the Landau-Zener formula

$$\langle I_z \rangle = \pm \frac{\gamma_e}{\gamma_n} \langle \rho_0 | \tilde{S}_z \rangle \left(1 - \exp\left(-\frac{\pi}{2} Q_{\text{crit}}^\mp\right) \right) \quad (19)$$

We note that it is impractical to vary the ω_{eff} indefinitely slow to maintain the high adiabaticity because relaxation effects will start impeding the transfers at long mixing times, i.e., each sample/experiment has to be individually optimized for maximum transfer. Nevertheless, the scaling factor a_\mp and the resonance conditions depend only on the pulse sequence, such that good initial guesses and sequence parameter ranges can be estimated theoretically.

III. MATERIALS AND METHODS

A. Numerical calculation of scaling factors

All numerical calculations were implemented in MATLAB (The MathWorks Inc). All sequences presented in

this work are piece-wise constant pulse sequences such that the effective fields could be calculated by quaternion multiplication of the individual pieces. Interaction-frame trajectories were calculated by time slicing. Fourier coefficients were calculated with an `fft` of $R^{(\text{eff})}(t)$. The two-dimensional simulation of BASE-DNP was implemented with the simulation package SPINACH⁴⁴. A three-spin electron-proton-proton system was used, with a \mathbf{g} -tensor of [2.0046 2.0038 2.0030], e-n distances of $r_1=4.5 \text{ \AA}$ and $r_2=6.5 \text{ \AA}$, polar angles of $\theta_1=0^\circ$ and $\theta_2=90^\circ$ and azimuthal angles $\phi_1=0^\circ$ and $\phi_2=70^\circ$. A simple T_1/T_2 relaxation theory was used, with $T_{1,e}=2.5 \text{ ms}$, $T_{2,e}=5 \text{ \mu s}$ and $T_{1,n}=36 \text{ s}$, $T_{2,n}=1 \text{ ms}$. Relaxation was implemented via the Levitt-Di Bari approach⁴⁵. A two-angle Lebedev grid⁴⁶ with 194 orientations was used.

B. Sample preparation

A 5 mM sample of OX063 trityl radical in DNP juice (glycerol- d_8 : D_2O : H_2O , 6:3:1 by volume) at 80 K was used for all experiments. In detail, 1.65 mg trityl radical (MW=1359 g mol⁻¹, 1.2 μmole) were dissolved in 24.3 μL of H_2O and 72.9 μL D_2O . Of the resulting solution, 48.6 μL were then added to 72.9 μL of gly- d_8 . 40 μL of the final solution were transferred to a 3 mm OD quartz capillary and flash frozen in liquid nitrogen before the measurements.

C. Instrumentation and EPR/NMR spectroscopy

All experimental data were acquired on a new home-built X-band spectrometer which is based on the design described in Ref.(⁴⁷). Notable differences for the experiments described in this work were that a 1.8 GSa/s digitizer (SP Devices ADQ412) was used and that the temperature of 80 K was achieved with a cryogen-free cryostat (Cryogenic Limited). Microwave pulses were generated with an arbitrary waveform generator (AWG) model M8190A (Keysight) and amplified with a 1 kW traveling wave tube (TWT) amplifier (Applied Systems Engineering). A standard Bruker EN4118A-MD4 ENDOR resonator was used, with an external rf tuning and matching circuit. NMR experiments were performed using a Stelar PC-NMR spectrometer. An Arduino board was used to count TWT gate triggers of the EPR spectrometer, each corresponding to an h increment (Fig. 3), and the Arduino board triggers the NMR acquisition after h loops.

FT EPR spectra were acquired by a chirp echo sequence with linear chirp pulses spanning 300 MHz, a duration of 200 ns ($\pi/2$) and 100 ns (π) and an inter-pulse delay of 2 μs . All EPR and NMR signals were processed in MATLAB. All experimental results presented in this work were acquired within a single session, i.e., the sample was not moved between different DNP experiments.

D. Pulse sequences and enhancements

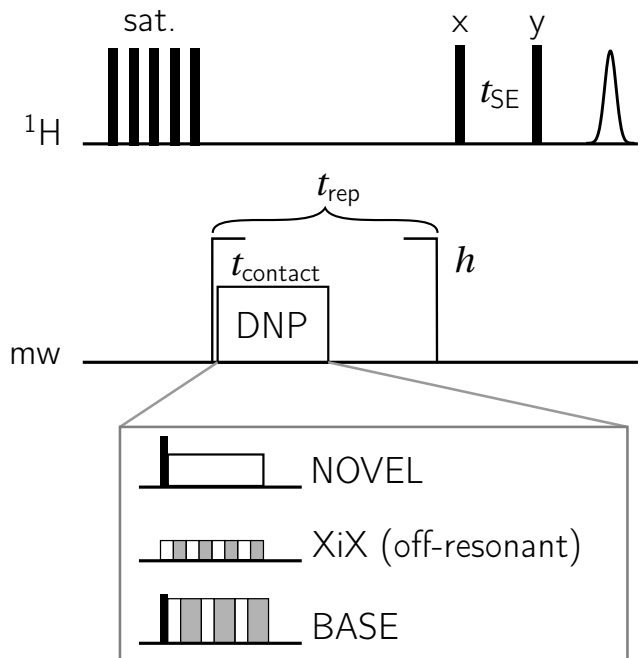


FIG. 3. General pulsed DNP sequence with various building blocks (NOVEL, XiX, and BASE) repeated by h loops before ^1H -NMR detection with a solid echo.

The basic structure of all DNP experiments, as addressed individually in the following section, is shown in Figure 3. A train of ^1H saturation pulses (eleven 100° pulses spaced by 1 ms) was applied before the DNP element. Each DNP block was repeated h times, with a total build-up time $T_{\text{DNP}} = h \cdot t_{\text{rep}}$. The contact time t_{contact} , during which the microwaves are turned on, is generally much shorter than the repetition time t_{rep} , due to a 1% duty cycle limit of the TWT. The ^1H NMR signal was then read out with a solid echo sequence comprised of two 2.5 μs 90° pulses separated by a delay of $t_{\text{SE}}=80 \text{ \mu s}$. A conventional eight-step phase cycle was used with $\{x, x, y, y, -x, -x, -y, -y\}$ for the first pulse and detection and $\{y, -y, x, -x, y, -y, x, -x\}$ for the second pulse. The proton spectrum at thermal equilibrium was acquired using similar parameters except without microwaves, and a delay of $180 \text{ s} \approx 5 \cdot T_{1,n}$ was used in between the 660 accumulated scans. The $T_{1,n}=36 \text{ s}$ was determined both with a saturation recovery sequence, and by the decay of polarization after DNP (see SI).

For most cases, we report the *polarization enhancement* ε_P , given by the ratio of the DNP-enhanced signal intensity divided by the signal intensity at thermal equilibrium. These values can be different from simple mw on/off signal enhancements recorded with the same delay, because the DNP build-up time T_B can be much shorter than $T_{1,n}$. For most parameter optimizations, we used a

repetition time t_{rep} of 1 ms, and a build-up time T_{DNP} of 2 s. Build-up curves were acquired by changing the value of h , and with variable repetition times mentioned in the respective figures.

IV. RESULTS

In this section, we apply the theory and design procedures outlined earlier for DNP experiments at X-band frequencies (9.5 GHz) using both low-power and high-power microwaves. The former involves variants of the recently published XiX-DNP experiments³⁰, while the latter involves development of a new pulse sequence with improved performance relative to previous NOVEL-DNP experiments^{18,19,21}.

A. Low-power XiX-DNP

Figure 4(a) shows the mw part of the XiX-DNP pulse sequence consisting of two oppositely phased pulses repeated n times, leading to a total contact time of $t_{\text{contact}} = n \cdot \tau_m = n \cdot (t_{p,1} + t_{p,2})$. Assuming an mw field with an amplitude of $\nu_1 = 4$ MHz (we use ω for angular frequencies and $\nu = \omega/2\pi$ for linear frequencies), and an offset slightly above 40 MHz, $t_{p,1} = t_{p,2} = 9$ ns, this leads to the calculated transfer profiles shown in Figure 4(b) when using fully numerical simulations (black circles), the full first-order Hamiltonian (blue), partial ZQ/DQ Hamiltonians (Eq. (9), red), or Taylor-expanded series (Eq. (16), green). The offset-dependent resonance conditions become clear in Figure 4(c) showing the electron and nuclear effective fields and the matching conditions. In this example, $\nu_{\text{eff}}^{(I)} = \nu_I$ and $k_I = 0$ for all resonance conditions. Since low-power mw irradiation is used, the electron effective field is mainly dominated by the electron offset. We note the reflection at $\nu_m/2$, which is a consequence of our particular choice of convention.

Figure 4(d) shows the experimental results and calculated f_{\mp} (Equation (17)) for different combinations of $t_{p,1}$ and $t_{p,2}$ (but with a constant sum $t_{p,1} + t_{p,2}$). The bottom case with $t_{p,1} = t_{p,2}$ corresponds to the sequence introduced by Mathies et al.³⁰. Clearly, both the positions and the relative intensities of the matching conditions are well predicted. The small peaks visible in the experimental data correspond to a three-spin electron-¹H-¹H transition (see SI). Interestingly, if both pulses have the same length (the bottom trace in Figure 4(d)), the resonance condition at the usual SE offset ($\Omega_S/2\pi \approx \nu_I$) is still fulfilled, but the scaling factor is zero. This figure shows that the resonance conditions alone are not enough to characterize the DNP performance and that the theoretical scaling factors reliably predict the relative DNP enhancement.

The performance of the XiX-DNP experiment may be further improved by adiabatically sweeping the effective fields through the resonance condition, i.e., slowly

increase $t_{p,2}$ upon increasing the loop number n (Figure 4(a)). The improved enhancement is demonstrated in DNP experiments (Figure 5(a)), where the adiabatic version of XiX-DNP with the second pulse swept from 8–10 ns (red line) clearly outperforms its diabatic counterpart proposed by Mathies and coworkers³⁰ (black line). Figure 5(b) shows the time-dependence of the effective field mismatch $\Delta\omega_{\text{eff}}^-(t)$ for the diabatic and adiabatic variants. The black lines correspond to the diabatic variant with fixed timing. Exactly at the offset of 40.89 MHz, the effective field mismatch is exactly zero (black solid line), and it does not change over time. Under these conditions, the transfer is optimal. However, if the offset is 2 MHz off — a reasonable value given that the FWHM of trityl is ~ 5 MHz — the effective fields are also mismatched by about 2 MHz (black dashed line). Consequently, the DNP matching condition is not fulfilled and the DNP transfer is entirely quenched for a system with small hyperfine couplings. On the contrary, it is evident that the effective field of the adiabatic variant (red) crosses zero in both cases, leading to polarization transfer for a broader distribution of electron offsets. Finally, Figure 5(c) shows the experimental build-up curve of the two XiX-DNP sequences, which clearly shows the advantages of implementing adiabatic XiX-DNP.

B. High-power BASE-DNP

We will now analyze pulsed DNP sequences requiring high-power mw irradiation. In particular, we examine NOVEL (nuclear orientation via spin locking)^{18–20} and its adiabatic version, the ramped-amplitude RA-NOVEL-DNP²¹ (Figure 6(a)). We will then show how a simple amplitude modulation can be used to improve its bandwidth.

For NOVEL, the spinlock strength has to match the nuclear Zeeman frequency, $\nu_1 \approx \nu_I$, while for RA-NOVEL the nutation frequency is slowly increased from below the matching condition to above it in a linear fashion. Although other amplitude modulation regimes were examined, no major improvement was observed at long contact times²¹. Figure 6(b) and (c) compare the DNP performances of the NOVEL sequences as function of the (average) Rabi field ν_1 and the offset $\Omega_S/2\pi$. The plots show that RA-NOVEL is more tolerant towards ν_1 mismatch, and hence leads to higher DNP enhancements. Additionally, the calculated mismatch plot (Figure 6(d)) also predicts that the adiabatic sequence can moderately improve the bandwidth for small couplings. Nevertheless, RA-NOVEL experiments did not show an improved offset compensation, most likely due to the more dominant mw Rabi field inhomogeneity (about 18%) across the sample.

Motivated by these results and also our previous works in designing broadband ssNMR recoupling sequences⁴⁸, we hypothesized that a broadband pulsed DNP sequence can be designed by combining XiX and NOVEL, i.e.,

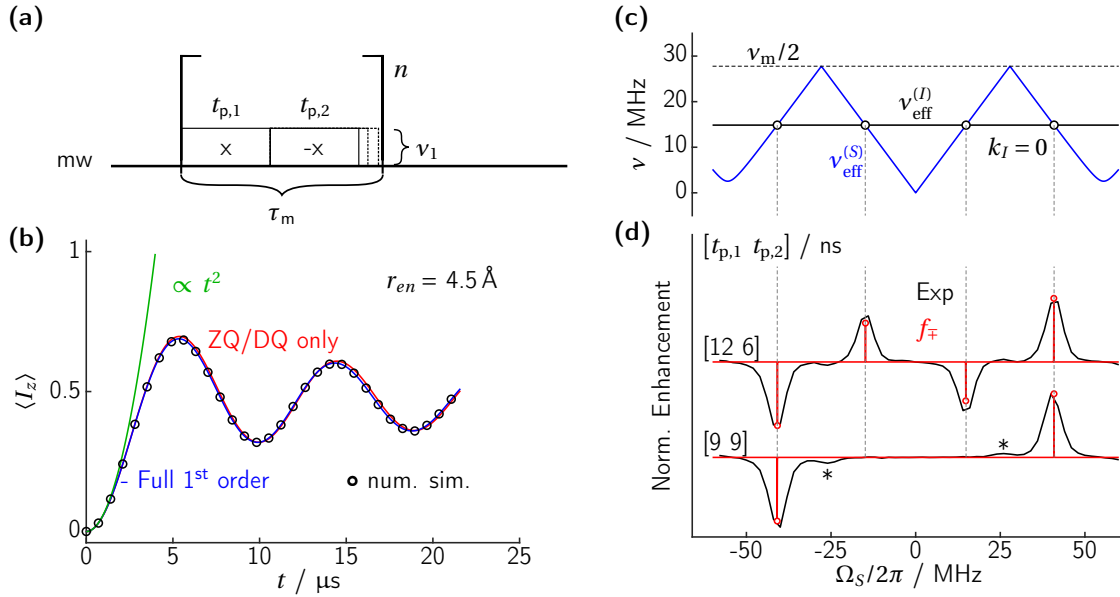


FIG. 4. Numerical and experimental analysis of the XiX-DNP experiment. (a) Pulse sequence for the mw part of the DNP experiment. (b) Comparison of $\tilde{S}_z \rightarrow I_z$ polarization transfer efficiencies calculated using an effective Hamiltonian including all first order terms (blue) or only the flip-flop terms (red) with a full numerical simulation (black circles). A two-spin $e^{-1}\text{H}$ spin pair with a distance $r_{en} = 4.5 \text{ \AA}$ is used in the numerical simulations. The green line illustrates the initial build-up in Equation (16). (c) and (d) Resonance conditions and theoretical and experimental enhancements for XiX-DNP with $\nu_1 = 4 \text{ MHz}$, $t_{\text{contact}} = 8 \text{ \mu s}$, $\tau_{\text{rep}} = 1 \text{ ms}$, $T_{\text{DNP}} = 2 \text{ s}$ as function of the electron offset frequency. (c) The absolute value of the effective fields $\nu_{\text{eff}}^{(S)}$ (blue) and $\nu_{\text{eff}}^{(I)}$ (black) as a function of the mw offset, for $t_{p,1} = t_{p,2} = 9 \text{ ns}$. Resonance conditions are indicated as black circles. (d) Experimental enhancements for different combinations of $t_{p,1}$ and $t_{p,2}$ (given in brackets) with fixed total modulation period (black), and theoretical predictions based on Equation (17) (red). Small additional peaks are due to higher-order processes involving two protons. The calculation in (b) was done at an electron offset of 40.89 MHz.

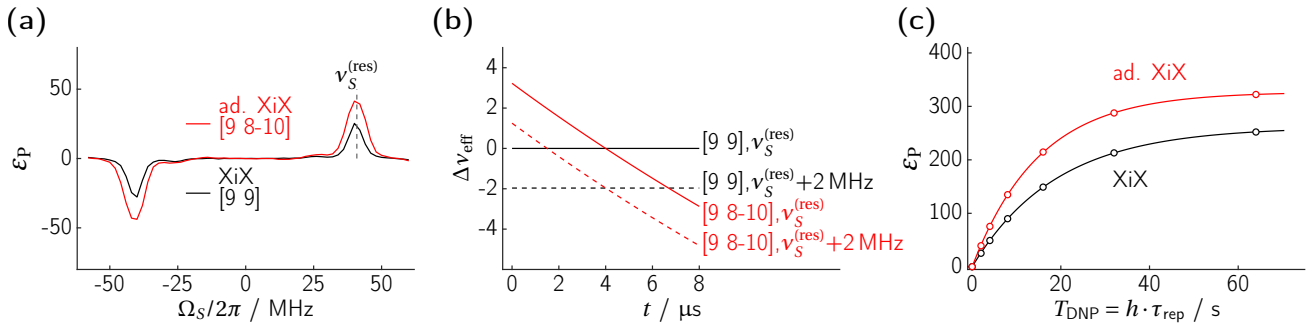


FIG. 5. Experimental comparison of the diabatic ($t_{p,1}=t_{p,2}=9 \text{ ns}$, black) and adiabatic ($t_{p,1}=9 \text{ ns}$, $t_{p,2}=8-10 \text{ ns}$, red) XiX-DNP. (a) XiX-DNP mw offset profile with 2s of buildup. (b) Mismatch between nuclear and electron effective fields for XiX (black) and its adiabatic version (red) as a function of contact time. Solid lines show an exactly-matched ($\Delta\nu_{\text{eff}} = 0$) resonance condition around 40 MHz, whereas the dashed line describes a scenario of a shifted resonance condition by 2 MHz. All lines except the black dashed line cross the $\Delta\nu_{\text{eff}} = 0$ line, and hence DNP will take place. This clearly shows the mismatch compensating feature exhibited by adiabatic sequences. (c) Experimental ^1H build-up curves with a repetition time of $t_{\text{rep}} = 1 \text{ ms}$. XiX-DNP: $\varepsilon_{\text{max}} = 261$, $T_{\text{B}} = 19.0 \text{ s}$, adiabatic XiX-DNP: $\varepsilon_{\text{max}} = 327$, $T_{\text{B}} = 15.1 \text{ s}$

a Broadband Amplitude modulated Signal Enhanced (BASE) DNP (Figure 7(a)). Similar to NOVEL (but unlike the XiX DNP), BASE-DNP is a spin-locked experiment. Additionally, the sequence can be made adiabatic by slowly varying $t_{p,2}$ through one of the matching conditions, which are shown as dashed lines in the 2D plot of a

theoretical prediction using Eq. (15) (Figure 7(c)). This calculation included distributions of electron offsets and Rabi fields. The intensity and width of the resonance conditions already hint at the robustness of them with respect to these parameters.

Figure 7(b) shows the DNP enhancement as a function

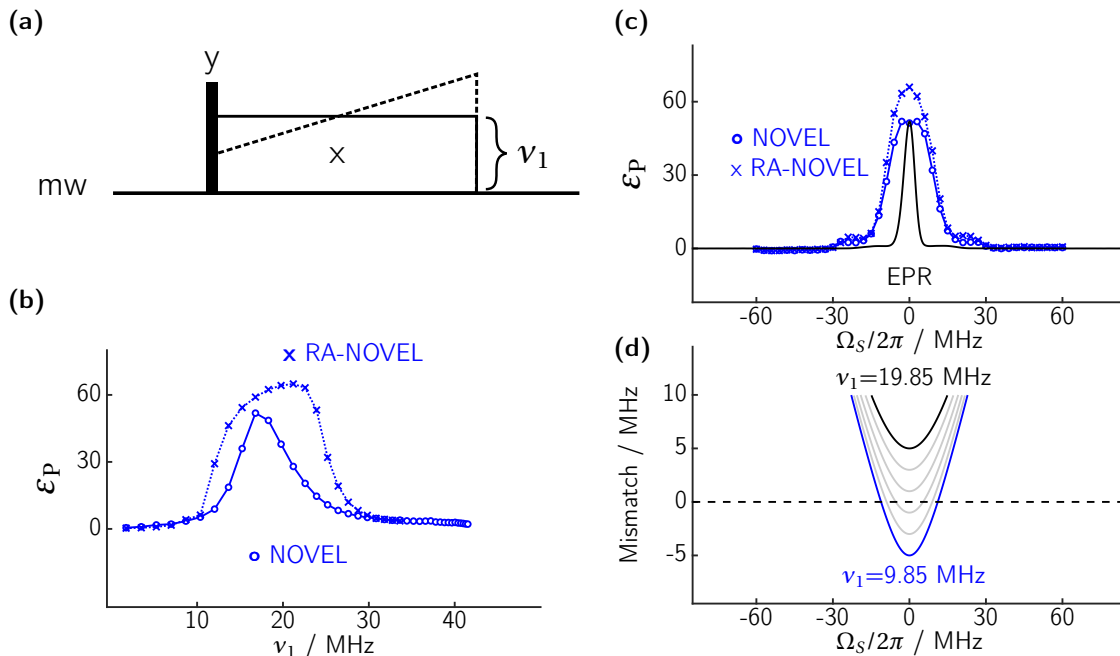


FIG. 6. **(a)** Pulse sequence for NOVEL and Ramped Amplitude (RA) NOVEL (dashed) DNP. **(b)** Experimental DNP enhancement as a function of the spin lock strength (Rabi frequency) ν_1 after 2 s of DNP. **(c)** DNP mw offset profiles for both NOVEL sequences (blue) and the EPR spectrum (black) with an arbitrary scale. **(d)** Calculated resonance mismatch (Eq. (13)) as a function of the offset for RA-NOVEL. The adiabatic sequence begins with a large negative $\Delta\nu_{\text{eff}} \ll 0$ (blue), which slowly increases towards $\Delta\nu_{\text{eff}} \sim 0$ (gray), and ends with a large positive $\Delta\nu_{\text{eff}} \gg 0$ (black). DNP occurs whenever the lines cross $\Delta\nu_{\text{eff}} = 0$.

of $t_{p,2}$ with a fixed value of $t_{p,1} = 20$ ns. One can see that the calculated f_{\mp} (Eq. (17)) matches the observed resonance conditions and the relative DNP performance well, despite the fact that the Rabi field inhomogeneity and mw offsets were simply neglected in these calculations. We have labeled the two different resonance conditions ($k_I = 0$ and $k_I = 1$) for later reference (*vide infra*), and the sweep range of the adiabatic variants are indicated by gray bars. The experimental enhancement as a function of both pulse lengths is shown in Figure 7(d). Again the positions of the resonance conditions are well predicted by the theory. There are some differences in the width and intensity that are expected from the simplistic two-spin model we are using. A slightly more sophisticated (though still simplistic) numerical calculation employing Spinach⁴⁴ is shown in Figure 7(e). Overall, our theory reliably predicts the resonance conditions for BASE-DNP. While numerical simulations of small spin systems can include more details, such as electronic relaxation, they are still not capturing all the complications in the complete DNP process. In this case, our (semi-)analytical theory is very helpful in quickly identifying resonance conditions and for choosing suitable experimental parameters.

We will now characterize the BASE-DNP resonance conditions in more detail. The DNP enhancement as a function of ν_1 is shown in Figure 8(a). It is evident that the adiabatic BASE outperforms its diabatic counterpart. For one of the resonance conditions, the best

transfer was achieved with the highest power available. A closer inspection at the $k_I = 0$ and $k_I = 1$ resonance conditions reveals that the position of the latter is much more robust with respect to the spin-lock field strength, in agreement with the experimental data (Figure 8(a)). Figure 8(b) shows the BASE DNP frequency profile (constant B_0 field with varying mw center frequency) for the $k_I = 1$ case. A maximum mw power was used for the $\pi/2$ pulse for a maximum bandwidth, but the spin-lock field was adjusted at each offset position according to the mw resonator (see SI). Note that the mw power adjustment was not possible for the adiabatic BASE due to the limited mw power available. The small enhancements at larger offsets ($\frac{\Omega_s}{2\pi} = \pm 60$ MHz) are due to the matched resonance conditions during the adiabatic sweep, where the offset-dependent mismatch during the contact period is explicitly calculated (Figure 8(c)).

As discussed in the analysis performed for RA-NOVEL, DNP occurs when the mismatch is zero (diabatic case) or passes zero (adiabatic case). The theory shows that the mismatch for BASE DNP is quite offset-tolerant, as visible in Figure 8(c). In other words, the mismatch hardly varies by more than 1 MHz over the $|\Omega_s/2\pi| < 30$ MHz range. Hence, the theory implies that BASE will be a broadband sequence, and indeed this was verified experimentally. It is evident that the increased Rabi field ν_1 employed in BASE has resulted in a $\sim 3\times$ higher bandwidth compared to RA-NOVEL

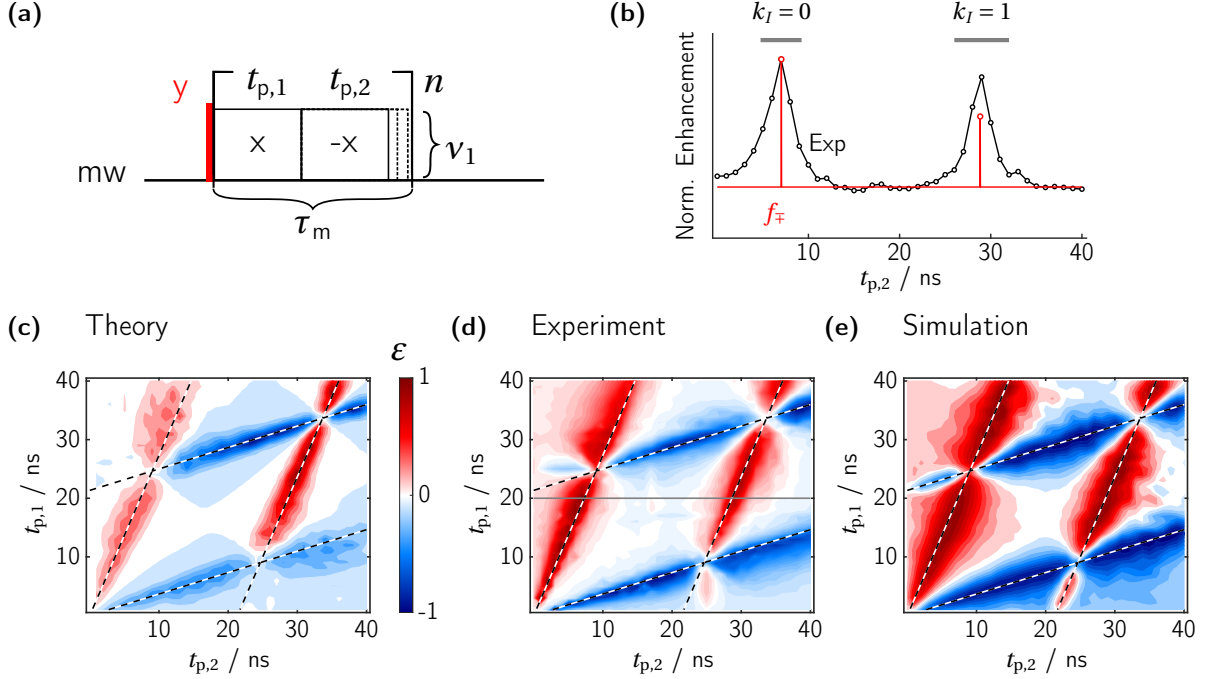


FIG. 7. (a) Pulse sequence of BASE-DNP. (b) Experimental (black) and calculated (red) DNP performance as a function of $t_{p,2}$ with fixed $t_{p,1}=20$ ns. The ranges for the adiabatic sweeps are marked by gray bars. (c) Calculated relative enhancement (Equation (10)) including offset distributions (5 MHz FWHM) and ν_1 inhomogeneity (6 MHz FWHM centered at 32 MHz). (d) Experimental BASE-DNP enhancement as a function of $t_{p,1}$ and $t_{p,2}$ with $T_{\text{DNP}}=1$ s. The observed resonance conditions matches well with the theory (black and white dashed lines). The solid gray line indicates the position of (b). (e) SPINACH simulation on a spin system described in Materials and Methods. The experiments were performed using on-resonance ($\Omega_S = 0$) mw irradiation and a Rabi field of $\nu_1 \sim 32$ MHz, which is twice of that used for NOVEL. Other experimental details include $t_{\text{contact}}=8 \mu\text{s}$, $\nu_1 \approx 32$ MHz, $t_{\text{rep}}=1$ ms.

(Figure 9). Moreover, we also measured the build-up curves (Figure 9(b)), and the results are summarized in Table I. In summary, adiabatic BASE has outperformed RA-NOVEL with a higher ε_{max} of ≈ 361 and $\varepsilon_{\text{max}} \cdot \sqrt{T_{1,n}/T_B} \approx 701$, compared to ε_{max} of ≈ 335 and $\varepsilon_{\text{max}} \cdot \sqrt{T_{1,n}/T_B} \approx 671$ for RA-NOVEL. Although the improvement of adiabatic BASE over RA-NOVEL is marginal ($\leq 8\%$), a larger relative gain can be envisaged when applied to other more generic DNP polarizing agents—which usually have broader lines than OX063, and, hence, offset compensation becomes critical.

V. CONCLUSIONS AND OUTLOOK

We have demonstrated a generalized theoretical treatment applicable to periodic DNP sequences in static samples. This is realized by analyzing the resonance conditions and determining the Fourier coefficients, which encode the details in a sequence — Rabi fields, phases, amplitudes, and mw offsets. We showed here an example of how theory can help design a broadband sequence that is robust against mw offsets. With further improvement by implementing adiabatic sweeps, we show that adiabatic BASE, to the best of our knowledge, is the best performing pulsed DNP sequence discovered to date.

TABLE I. Enhancements ε_{max} , build-up times T_B , and sensitivity per unit time (i.e., signal per square root of time) $\varepsilon_{\text{max}} \cdot \sqrt{T_{1,n}/T_B}$ for RA-NOVEL and adiabatic BASE. All measured with an additional flip-back pulse after the DNP contact. $T_{1,n} = 36.2$ s. $T_{1,e} = 2.5$ ms.

	RA-NOVEL	ad. BASE
$t_{\text{rep}} = 2$ ms		
ε_{max}	321	342
T_B / s	8.3	8.7
$\varepsilon_{\text{max}} \cdot \sqrt{\frac{T_{1,n}}{T_B}}$	671	701
$t_{\text{rep}} = 5$ ms		
ε_{max}	335	361
T_B / s	12.1	12.1
$\varepsilon_{\text{max}} \cdot \sqrt{\frac{T_{1,n}}{T_B}}$	580	626

This is supported by having obtained excellent enhancement values on trityl at static conditions, a temperature of 80 K and a field of 0.35 T — with ε_{max} of ≈ 361 and $\varepsilon_{\text{max}} \cdot \sqrt{T_{1,n}/T_B} \approx 701$, which are higher than RA-NOVEL. While the adiabatic solid effect²⁵ can achieve similar maximal enhancements of 360, it can only reach sensitivity enhancements of $\varepsilon_{\text{max}} \cdot \sqrt{T_{1,n}/T_B} \approx 629$ (see

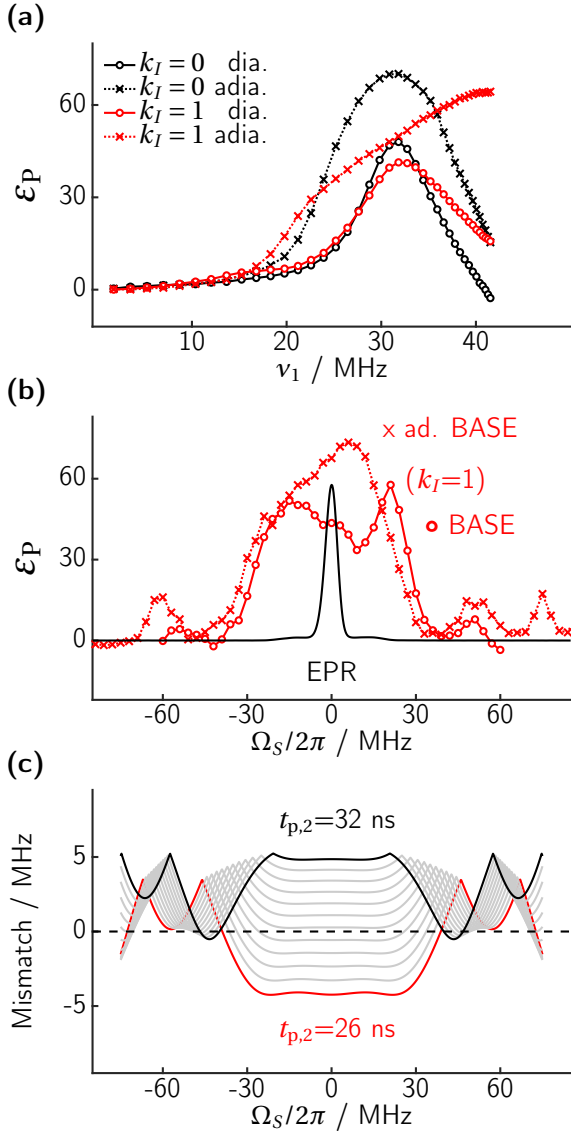


FIG. 8. Experimental BASE-DNP enhancement as a function of (a) the Rabi field ν_1 for the diabatic and adiabatic versions of the respective resonance conditions and (b) offset $\Omega_S/2\pi$, and an EPR spectrum is included here for reference (black). The BASE parameters were $t_{p,1} = 20$ ns, $t_{\text{contact}} = 8$ μs , $\tau_{\text{rep}} = 1$ ms, $T_{\text{DNP}} = 2$ s. The pulse length of the second pulse, $t_{p,2}$ was fixed in the case of (diabatic) BASE ('o') to 7 ns ($k_I = 0$) and 29 ns ($k_I = 1$), while it was swept over 4.75–9.25 ns ($k_I = 0$) or 26–32 ns ($k_I = 1$) for adiabatic BASE ('x'). (c) Calculated offset-dependent mismatch for $k_I = 1$ condition. The adiabatic sweep begins with $t_{p,2} = 26$ ns (red), through the intermediate stages (gray), and ends at $t_{p,2} = 32$ ns (black).

SI) and is inherently limited to a bandwidth equal to or lower than the nuclear Zeeman frequency.

Moreover, our theory implies that adiabatic BASE should have field-independent performances, provided that the mw Rabi fields are also scaled linearly with the external magnetic fields. Although the mw power requirement for adiabatic BASE currently cannot be ful-

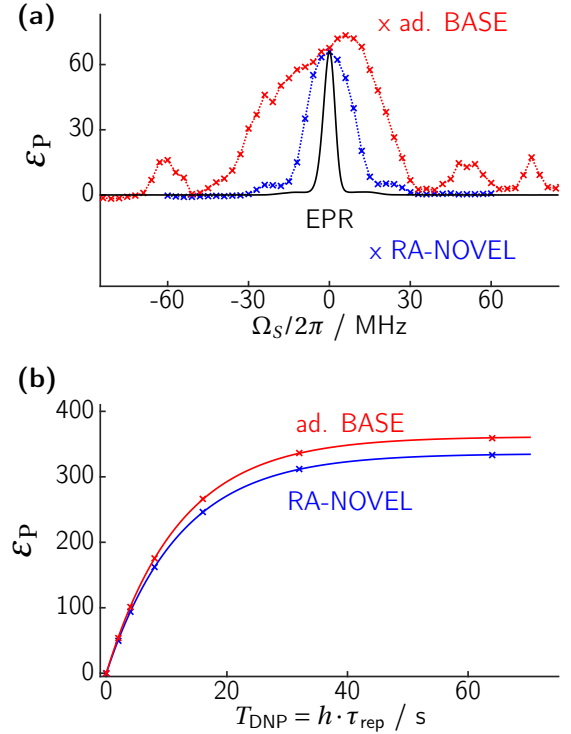


FIG. 9. (a) DNP frequency profile of RA-NOVEL and adiabatic BASE ($k_I = 1$) DNP with 2s build up time. (b) DNP build-up curve using a repetition time of 5 ms. The build-up curves were fitted with exponential functions $\varepsilon_P(T_{\text{DNP}}) = \varepsilon_{\text{max}}(1 - \exp(-T_{\text{DNP}}/T_B))$. The build-up curves were measured using different repetition times τ_{rep} 1–20 ms, where $t_{\text{rep}} = 5$ ms yield the largest ε , and $t_{\text{rep}} \sim 2$ ms resulted in the highest $\varepsilon_{\text{max}}/\sqrt{T_{1,n}/T_B}$. 90° flip-back pulses were applied after each DNP contact to replenish the electron Zeeman spin bath. Exact BASE parameters are given in Figure 8.

filled for high-field (> 5 T) DNP NMR applications, it could be satisfactorily fulfilled for polarizing ^{13}C in diamond nitrogen-vacancy (NV) centers. For example, PulsePol, which requires an order of magnitude more mw power than adiabatic BASE, was demonstrated to polarize ^{13}C nuclei in diamond NVs at ~ 0.17 T²⁸. In such situations, a broadband sequence that is robust against mw power inhomogeneity and offsets could be advantageous for quantum computing applications⁴⁹.

Lastly, we emphasize that our generalized theoretical framework is not only applicable to DNP sequences, it is also valid for other magnetic resonance applications. In fact, the framework developed in this paper is a direct adaptation (with minor adjustments) from NMR theory, as it has been applied to various recoupling and decoupling sequences. Hence, it is not too far-fetched to envision that our theoretical framework could be applied to electron paramagnetic resonance pulse sequences employing matching conditions^{50,51}, or to future pulsed MAS-DNP experiments.

AUTHOR CONTRIBUTIONS

NW, KOT, and GJ designed the research. NW performed all measurements with help from LAV and LS. NW, ABN and NCN developed the theory. All simulation scripts were written by NW, with general help and input from KOT, ABN and LAV.

ACKNOWLEDGMENTS

This article is dedicated to Dr. Anton Ashuiev, stranded in Ukraine at the time of writing. Dr. Daniel Klose and René Tschaggelar are acknowledged for building the EPR spectrometer used for this work. We thank Prof. Matthias Ernst and Prof. Robert G. Griffin for extensive and numerous discussions. Prof. Jan Henrik Ardenkjær-Larsen generously provided OX063 for an earlier project. KOT acknowledges the funding support from the French National Research Agency (ANR-20-ERC9-0008) and the Respire program (petit équipement projet n°339299). NW and GJ acknowledge funding by ETH Zürich grant ETH-48 16-1.

- ¹A. Abragam and M. Goldman, "Principles of dynamic nuclear polarisation," *Reports Prog. Phys.* **41**, 395–467 (1978).
- ²A. S. Lilly Thankamony, J. J. Wittmann, M. Kaushik, and B. Corzilius, "Dynamic nuclear polarization for sensitivity enhancement in modern solid-state NMR," *Prog. Nucl. Magn. Reson. Spectrosc.* **102-103**, 120–195 (2017).
- ³A. W. Overhauser, "Polarization of nuclei in metals," *Phys. Rev.* **92**, 411–415 (1953).
- ⁴J. H. Ardenkjær-Larsen, B. Fridlund, A. Gram, G. Hansson, L. Hansson, M. H. Lerche, R. Servin, M. Thaning, and K. Goldman, "Increase in signal-to-noise ratio of $> 10,000$ times in liquid-state NMR," *Proc. Natl. Acad. Sci.* **100**, 10158–10163 (2003).
- ⁵L. R. Becerra, G. J. Gerfen, R. J. Temkin, D. J. Singel, and R. G. Griffin, "Dynamic nuclear polarization with a cyclotron resonance maser at 5 T," *Phys. Rev. Lett.* **71**, 3561–3564 (1993).
- ⁶J. H. Ardenkjær-Larsen, S. Bowen, J. R. Petersen, O. Rybalko, M. S. Vinding, M. Ullisch, and N. C. Nielsen, "Cryogen-free dissolution dynamic nuclear polarization polarizer operating at 3.35 t, 6.70 t, and 10.1 t," *Magnetic Resonance in Medicine* **81**, 2184–2194 (2018).
- ⁷S. Jannin, J. N. Dumez, P. Giraudeau, and D. Kurzbach, "Application and methodology of dissolution dynamic nuclear polarization in physical, chemical and biological contexts," *J. Magn. Reson.* **305**, 41–50 (2019).
- ⁸K. O. Tan, S. Jawa, R. J. Temkin, and R. G. Griffin, "Pulsed dynamic nuclear polarization," *eMagRes* **8**, 339–352 (2019).
- ⁹P. Berruyer, S. Björgvinsdóttir, A. Bertarello, G. Stevanato, Y. Rao, G. Karthikeyan, G. Casano, O. Ouari, M. Lelli, C. Reiter, F. Engelke, and L. Emsley, "Dynamic nuclear polarization enhancement of 200 at 21.15 t enabled by 65 kHz magic angle spinning," *The Journal of Physical Chemistry Letters* **11**, 8386–8391 (2020).
- ¹⁰X. Cai, A. L. Paioni, A. Adler, R. Yao, W. Zhang, D. Beriashvili, A. Safeer, A. Gurinov, A. Rockenbauer, Y. Song, M. Baldus, and Y. Liu, "Highly efficient trityl-nitroxide biradicals for biomolecular high-field dynamic nuclear polarization," *Chemistry – A European Journal* **27**, 12758–12762 (2021).
- ¹¹A. Abragam and W. G. Proctor, "Une nouvelle methode de polarisation dynamique des noyaux atomiques dans les solides." *Comp. Rend. Acad. Sci.* **246**, 2253–2256 (1958).
- ¹²C. D. Jeffries, "Polarisation of Nuclei by Resonance Saturation in Paramagnetic Crystals," *Phys. Rev.* **106**, 164–165 (1957).
- ¹³C. F. Hwang and D. A. Hill, "New effect in dynamic polarization," *Phys. Rev. Lett.* **18**, 110–112 (1967).
- ¹⁴A. Kessenikh, V. Luschikov, A. Manekov, and Y. V. Taran, "Proton polarization in irradiated polyethylenes," *Sov. Physics-Solid State* **5**, 321–329 (1963).
- ¹⁵B. N. Provotorov, "Magnetic Resonance Saturation in Crystals," *Sov. Phys. JETP* **14**, 1126–1131 (1962).
- ¹⁶M. Borghini, "Spin-temperature model of nuclear dynamic polarization using free radicals," *Phys. Rev. Lett.* **20**, 419–421 (1968).
- ¹⁷J. Soetbeer, P. Gast, J. J. Walish, Y. Zhao, C. George, C. Yang, T. M. Swager, R. G. Griffin, and G. Mathies, "Conformation of bis-nitroxide polarizing agents by multi-frequency EPR spectroscopy," *Physical Chemistry Chemical Physics* **20**, 25506–25517 (2018).
- ¹⁸A. Henstra, P. Dirksen, J. Schmidt, and W. T. Wenckebach, "Nuclear spin orientation via electron spin locking (NOVEL)," *Journal of Magnetic Resonance* (1969) **77**, 389–393 (1988).
- ¹⁹T. V. Can, J. J. Walish, T. M. Swager, and R. G. Griffin, "Time domain DNP with the NOVEL sequence," *J. Chem. Phys.* **143**, 054201 (2015).
- ²⁰G. Mathies, S. Jain, M. Reese, and R. G. Griffin, "Pulsed Dynamic Nuclear Polarization with Trityl Radicals," *J. Phys. Chem. Lett.* **7**, 111–116 (2016).
- ²¹T. V. Can, R. T. Weber, J. J. Walish, T. M. Swager, and R. G. Griffin, "Ramped-amplitude NOVEL," *J. Chem. Phys.* **146**, 154204 (2017).
- ²²S. K. Jain, G. Mathies, and R. G. Griffin, "Off-resonance NOVEL," *J. Chem. Phys.* **147**, 164201 (2017).
- ²³A. Henstra, P. Dirksen, and W. T. Wenckebach, "Enhanced dynamic nuclear polarization by the integrated solid effect," *Phys. Lett. A* **134**, 134–136 (1988).
- ²⁴T. V. Can, R. T. Weber, J. J. Walish, T. M. Swager, and R. G. Griffin, "Frequency-Swept Integrated Solid Effect," *Angew. Chemie - Int. Ed.* **56**, 6744–6748 (2017).
- ²⁵K. O. Tan, R. T. Weber, T. V. Can, and R. G. Griffin, "Adiabatic Solid Effect," *J. Phys. Chem. Lett.* **11**, 3416–3421 (2020).
- ²⁶R. A. Wind, L. Li, H. Lock, and G. E. Maciel, "Dynamic nuclear polarization in the nuclear rotating frame," *J. Magn. Reson.* **79**, 577–582 (1988).
- ²⁷V. Weis, M. Bennati, M. Rosay, and R. G. Griffin, "Solid effect in the electron spin dressed state: a new approach for dynamic nuclear polarization," *J. Chem. Phys.* **113**, 6795–6802 (2000).
- ²⁸I. Schwartz, J. Scheuer, B. Tratzmiller, S. Müller, Q. Chen, I. Dhand, Z.-Y. Wang, C. Müller, B. Naydenov, F. Jelezko, and M. B. Plenio, "Robust optical polarization of nuclear spin baths using hamiltonian engineering of nitrogen-vacancy center quantum dynamics," *Science Advances* **4**, eaat8978 (2018).
- ²⁹K. O. Tan, C. Yang, R. T. Weber, G. Mathies, and R. G. Griffin, "Time-optimized pulsed dynamic nuclear polarization," *Science Advances* **5**, eaav6909 (2019).
- ³⁰V. S. Redrouthu and G. Mathies, "Efficient pulsed dynamic nuclear polarization with the x-inverse-x sequence," *Journal of the American Chemical Society* **144**, 1513–1516 (2022).
- ³¹R. Shankar, M. Ernst, P. K. Madhu, T. Vosegaard, N. C. Nielsen, and A. B. Nielsen, "A general theoretical description of the influence of isotropic chemical shift in dipolar recoupling experiments for solid-state NMR," *The Journal of Chemical Physics* **146**, 134105 (2017).
- ³²A. B. Nielsen, M. R. Hansen, J. E. Andersen, and T. Vosegaard, "Single-spin vector analysis of strongly coupled nuclei in TOCSY NMR experiments," *The Journal of Chemical Physics* **151**, 134117 (2019).
- ³³J. P. Wolfe, "Direct Observation of a Nuclear Spin Diffusion Barrier," *Phys. Rev. Lett.* **31**, 907–910 (1973).
- ³⁴K. O. Tan, M. Mardini, C. Yang, J. H. Ardenkjær-Larsen, and R. G. Griffin, "Three-spin solid effect and the spin diffusion barrier in amorphous solids," *Sci. Adv.* **5**, eaax2743 (2019).

- ³⁵S. K. Jain, C. J. Yu, C. B. Wilson, T. Tabassum, D. E. Freedman, and S. Han, "Dynamic Nuclear Polarization with Vanadium(IV) Metal Centers," *Chem* **7**, 421–435 (2021).
- ³⁶Q. Stern, S. F. Cousin, F. Mentink-Vigier, A. C. Pinon, S. J. Elliott, O. Cala, and S. Jannin, "Direct observation of hyperpolarization breaking through the spin diffusion barrier," *Sci. Adv.* **7**, 1–14 (2021).
- ³⁷B. Blümich and H. W. Spiess, "Quaternions as a practical tool for the evaluation of composite rotations," *J. Magn. Reson.* **61**, 356–362 (1985).
- ³⁸C. Counsell, M. Levitt, and R. Ernst, "Analytical theory of composite pulses," *Journal of Magnetic Resonance* (1969) **63**, 133–141 (1985).
- ³⁹K. O. Tan, M. Rajeswari, P. K. Madhu, and M. Ernst, "Asynchronous symmetry-based sequences for homonuclear dipolar recoupling in solid-state nuclear magnetic resonance," *J. Chem. Phys.* **142**, 1–9 (2015).
- ⁴⁰S. Vega, "Fictitious spin 1/2 operator formalism for multiple quantum NMR," *The Journal of Chemical Physics* **68**, 5518–5527 (1978).
- ⁴¹A. Wokaun and R. R. Ernst, "Selective excitation and detection in multilevel spin systems: Application of single transition operators," *The Journal of Chemical Physics* **67**, 1752–1758 (1977).
- ⁴²J. Baum, R. Tycko, and A. Pines, "Broadband and adiabatic inversion of a two-level system by phase-modulated pulses," *Phys. Rev. A* **32**, 3435–3447 (1985).
- ⁴³G. Jeschke, S. Pribitzer, and A. Doll, "Coherence Transfer by Passage Pulses in Electron Paramagnetic Resonance Spectroscopy," *J. Phys. Chem. B* **119**, 13570–13582 (2015).
- ⁴⁴H. Hogben, M. Krzystyniak, G. Charnock, P. Hore, and I. Kuprov, "Spinach – a software library for simulation of spin dynamics in large spin systems," *Journal of Magnetic Resonance* **208**, 179–194 (2011).
- ⁴⁵M. H. Levitt and L. D. Bari, "Steady state in magnetic resonance pulse experiments," *Physical Review Letters* **69**, 3124–3127 (1992).
- ⁴⁶V. Lebedev and D. Laikov, "Quadrature formula for the sphere of 131-th algebraic order of accuracy," *Dokl. Akad. Nauk SSSR* **366**, 741–745 (1999).
- ⁴⁷A. Doll and G. Jeschke, "Wideband frequency-swept excitation in pulsed EPR spectroscopy," *Journal of Magnetic Resonance* **280**, 46–62 (2017).
- ⁴⁸K. O. Tan, A. B. Nielsen, B. H. Meier, and M. Ernst, "Broadband DREAM recoupling sequence," *The Journal of Physical Chemistry Letters* **5**, 3366–3372 (2014).
- ⁴⁹J. Scheuer and B. Naydenov, "Dynamic nuclear polarization (DNP) in diamond," in *Diamond for Quantum Applications Part 1* (Elsevier, 2020) pp. 277–293.
- ⁵⁰G. Jeschke, R. Rakhmatullin, and A. Schweiger, "Sensitivity Enhancement by Matched Microwave Pulses in One- and Two-Dimensional Electron Spin Echo Envelope Modulation Spectroscopy," *Journal of magnetic resonance* **131**, 261–271 (1998).
- ⁵¹R. Rizzato, I. Kaminker, S. Vega, and M. Bennati, "Cross-polarisation edited ENDOR," *Mol. Phys.* **111**, 2809–2823 (2013).

Supporting Information for: Designing Broadband Pulsed Dynamic Nuclear Polarization Sequences in Static Solids

Nino Wili¹, Anders Bodholt Nielsen², Laura Alicia Völker¹, Lukas Schreder¹, Niels Chr. Nielsen², Gunnar Jeschke¹ and Kong Ooi Tan³

¹ *Department of Chemistry and Applied Biosciences, Laboratory of Physical Chemistry, ETH Zurich, Vladimir-Prelog-Weg 2, 8093 Zurich, Switzerland. E-mail: nino.wili@alumni.ethz.ch*

² *Interdisciplinary Nanoscience Center (iNANO) and Department of Chemistry, Aarhus University, Gustav Wieds Vej 14, DK-8000 Aarhus C, Denmark*

³ *Laboratoire des Biomolécules, LBM, Département de Chimie, École Normale Supérieure, PSL University, Sorbonne Université, CNRS, 75005 Paris, France. E-mail: kong-ooi.tan@ens.psl.eu*

Contents

S.1	Calculation of Fourier coefficients and scaling factors for BASE	2
S.2	Comparison of numerical and analytical computations for strongly coupled protons	11
S.3	Three-spin transitions	12
S.4	Resonator profile	13
S.5	Experimental data for the adiabatic solid effect (ASE)	14
S.6	Experimental determination of $T_{1,e}$	15
S.7	Experimental determination of $T_{1,n}$	16

S.1 Calculation of Fourier coefficients and scaling factors for BASE

In this section, we show an example of how to calculate the effective fields and scaling factors on the example of BASE. Although BASE is best applied on-resonant, we include here an offset of 5 MHz for illustration. The example can be found in the file `DNPexample_BASE.m`.

S.1.1 Build the rf-irradiation

```
1 clear, close all
2
3 % add helper functions
4 addpath(genpath('./core/'))
5
6
7 %% define sequence parameters
8 nu_I=-14.83;           % Nuclear Zeeman frequency
9 nu_1=32;              % Electron Rabi freq
10 tp1=20*1e-3;        % first pulse length in BASE
11 tp2=(1+tp1*(nu_1-abs(nu_I)))/(abs(nu_I)+nu_1); % second pulse
    length in BASE
12
13
14 nul_vec = nu_1*[1 1];
15 tp_vec = [tp1 tp2];
16 phi_vec = [0 180]/180*pi; % phases of the pulses
17 dt =0.1e-4;         % time step of numerical IFT
18
19 offset = 5;
20
21 rho0_vec = [-1 0 0]';
22
23 %% build rf
24 [ rf, time ]=build_rf(tp_vec,nul_vec,phi_vec,dt);
25
26 %plotting
27 h = figure(1);
28 clf
29 hold on
30 plot(time*1e3,real(rf),'b')
31 plot(time*1e3,imag(rf),'r')
32 xlabel('t / ns')
33 ylabel('\nu_1 / MHz')
34 axis([-1 60 -40 40])
```

35 `legend('real(rf)', 'imag(rf)', 'location', 'northeast')`

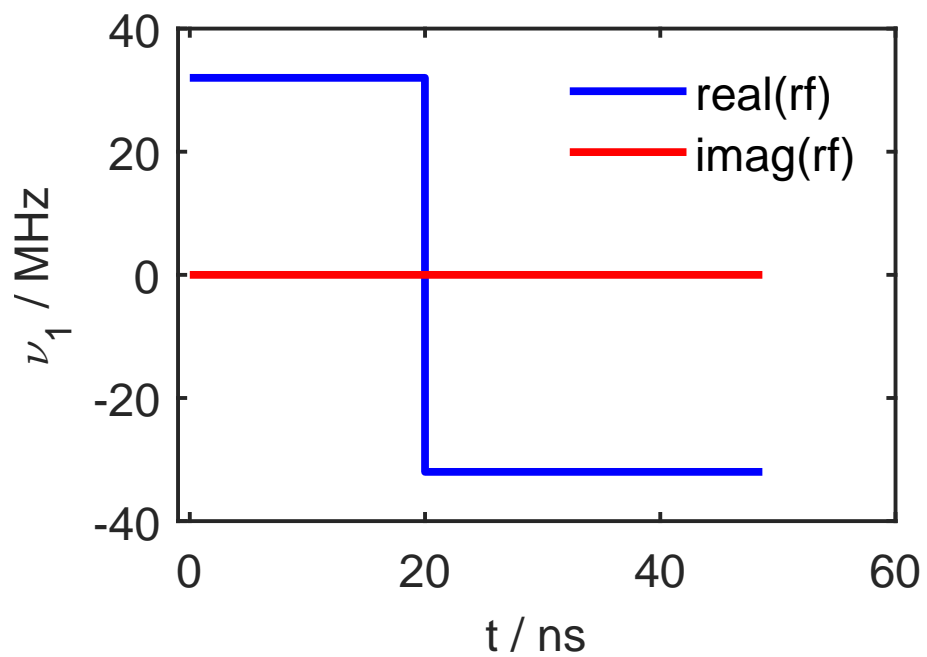


Fig. S1: rf-irradiation scheme for the BASE simulation.

S.1.2 Calculate $R^{(\text{control})}(t)$

```
42 % generate a vector of offsets the same length as rf
43 offset=offset*ones(size(rf));
44
45 %calculate modulation frequency
46 wmod=2*pi/(time(end)+dt);
47 nu_m = wmod/2/pi;
48
49
50 % pre-allocate rotation matrices
51 R_control = zeros(3,3,numel(time));
52 R_flipped = zeros(3,3,numel(time));
53
54
55 % build array of rotation quaternions for every step
56 q_pulse = zeros(4,numel(time));
57 for it = 1:numel(time)
58     q_pulse(:,it)=quat_rf(abs(rf(it)),angle(rf(it)),offset(it),dt,'frame'
59         ) ;
60
61
62 % multiply the quaternionas step-by-step and
63 % express them as an array of rotation matrices (for plotting only at
64     this stage)
65 qtot = [1 0 0 0]';
66 q_control = zeros(4,numel(time));
67 for it=1:numel(time)
68     q_control(:,it)=qtot;
69     R_control(:, :, it) = quat2rotmat(qtot);
70     qtot = quatmult(qtot,q_pulse(:,it));
71
72
73
74 % Plot IF in rotating frame
75 IF_plot(time,R_control,2);
```

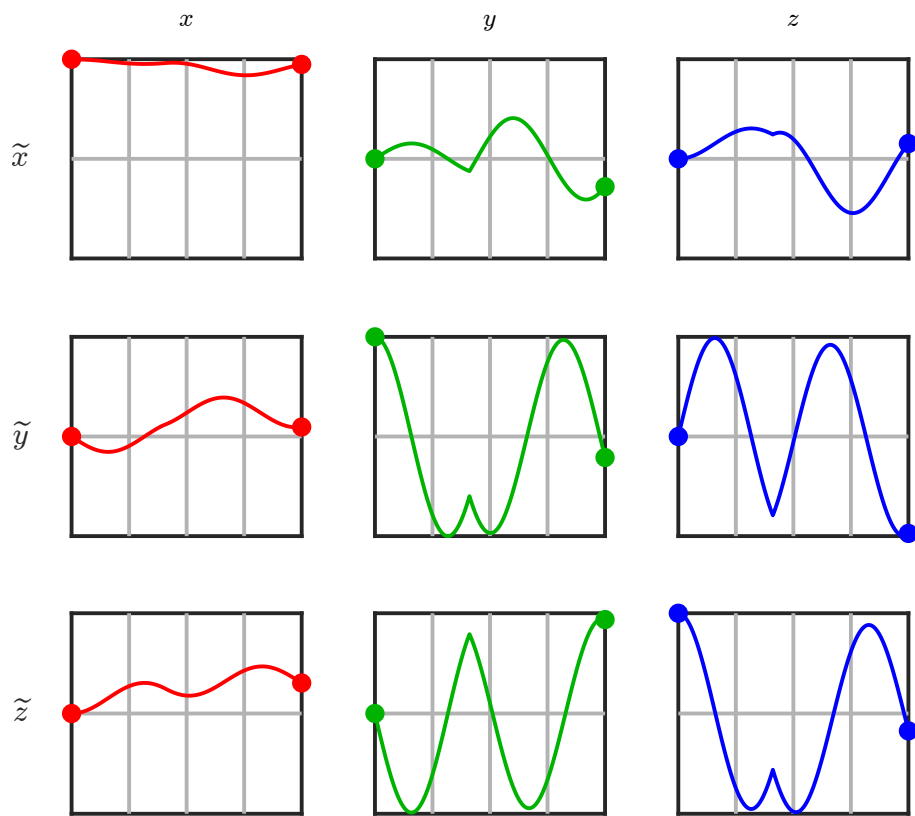


Fig. S2: Time-dependence of each element of $R^{(\text{control})}(t)$.

S.1.3 Remove the effective field from $R^{(\text{control})}(t)$, determine $R^{(\text{eff})}(t)$

```
82 %% flip each quaternion of q_control (or R_control)
83 % such that the effective field is now along the z-axis
84
85 %determine the effective field (effective flip angle and direction)
86 [z_eff,beta_eff] = quat2eff(qtot);
87
88 % determine R_flip, or the corresponding quaternion, respectively
89 % see https://doi.org/10.1063/1.5123046 for details
90 u_z = [0 0 1]';
91 q_flip = cross(z_eff,u_z);
92 qr_flip = 1+u_z'*z_eff;
93 q_flip = [qr_flip; q_flip ];
94 q_flip = q_flip/sqrt(sum(q_flip'*q_flip));
95
96 % flip all quaternions/rot-matrices
97 q_flipped= zeros(4,numel(time));
98 for it=1:numel(time)
99     q_flipped(:,it)=quatmult(q_flip,q_control(:,it));
100     R_flipped(:, :,it) = quat2rotmat(q_flipped(:,it));
101 end
102
103 %% remove the effective field from the IFT, i.e. calculate R_eff(t)
104 % determine the effective field frequency
105 w_eff = beta_eff/(time(end)+dt);
106 nu_eff = w_eff/(2*pi);
107
108 %pre-allocate rotation quaternions/matrices
109 q_eff = zeros(4,numel(time));
110 R_eff = zeros(3,3,numel(time));
111
112 % calculate R_eff(t)
113 for it=1:numel(time)
114
115     %calculate Rz(-w_eff*t),
116     beta = -w_eff*time(it);
117     q_z = [cos(beta/2) sin(beta/2)*[0 0 1]]';
118
119     q_eff(:,it)=quatmult(q_z,q_flipped(:,it));
120     R_eff(:, :,it) = quat2rotmat(q_eff(:,it));
121 end
122
```

123 IF_plot (time, R_eff, 3);

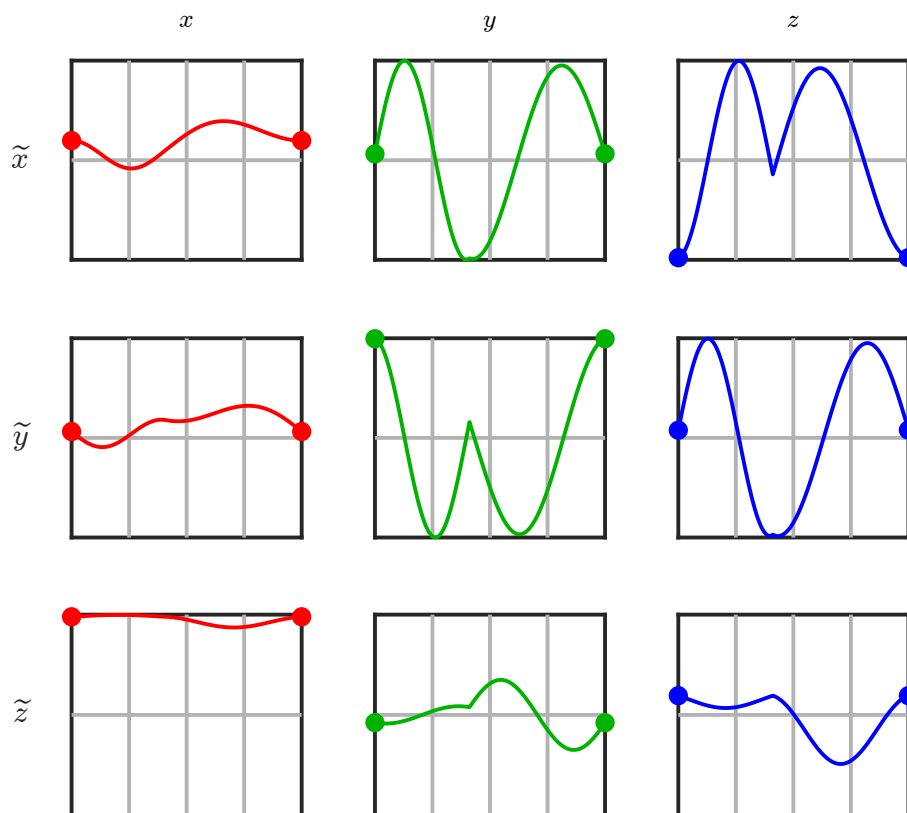


Fig. S3: Time-dependence of each element of $R^{(\text{eff})}(t)$. Note that all elements are preiodic.

S.1.4 Calculate the Fourier coefficients and scaling factors

```
128 %% calculate Fourier coefficients a^(k)
129 N=numel(time);
130 k_vec = ((0:N-1)-fix(N/2));
131 if mod(N,2)==0
132     k_vec = k_vec(2:end);
133 end
134
135 A_k = zeros(3,3,numel(k_vec));
136
137
138 % Fourier transform each element (xx,xy,xz,...zz) of R_eff(t)
139 for ii=1:3
140     for jj=1:3
141         y = squeeze(R_eff(ii,jj,:));
142         a = fftshift(fft(y))/numel(y);
143         if mod(N,2)==0
144             A_k(ii,jj,:)=a(2:end);
145         else
146             A_k(ii,jj,:)=a(1:end);
147         end
148     end
149 end
150
151
152 %extract the original z operator (should no oszillate during free
    evolution)
153 Az_k = squeeze(A_k(:,3,:));
154
155 %% extract the relevant scaling factor
156
157 [nu_eff_I,kI] = get_nu_eff_I(nu_I,nu_m);
158
159 kmax=max(k_vec);
160
161 ax = squeeze(Az_k(1,:));
162 ay = squeeze(Az_k(2,:));
163 ap = ax-1i*ay;
164 am = ax+1i*ay;
165 az = squeeze(Az_k(3,:));
166
167
```

```

168 k0 = kmax+1;
169 k = kmax+1+kI;
170 mk = kmax+1-kI;
171
172 rel_sign = sign(nu_eff*nu_eff_I);
173 if rel_sign == 1
174     a_eff= -sqrt(ap(mk)*am(k)) ;
175 else
176     a_eff= sqrt(am(mk)*ap(k)) ;
177 end
178
179 proj = z_eff'*rho0_vec;
180
181 f_pm = a_eff*proj

```

S.1.5 Compare with fully numerical calculation

```

183 %% comparison with numerical simulation
184
185 Ntheta = 31; %number of orientations
186
187 r=4.5; % e-n distance in Angstrom
188 Nrounds = 200; %number of repetitions of the DNP element
189
190 %caluclate the transfer numerically
191 [t_num,sig_num]=DNP_numerical(tp_vec,phi_vec,nul_vec,offset,nu_I,rho0_vec
    ,r,Ntheta,Nrounds);
192
193 h4=figure(4);
194 clf
195 hold on
196 plot(t_num,sig_num)
197
198 %% analytical calculation
199 %calculate the mismatch
200 delta_nu_eff = abs(nu_eff_pieewise(tp_vec,phi_vec,nul_vec,offset))-abs(
    nu_eff_I);
201
202 %calculate the anisotropy of the hf-coupling
203 natural_constants
204 T = mu0/(4*pi)*gfree*bmagn*g1H*nmagn*1/(r*1e-10)^3/planck/1e6;
205
206 %generate orientations and corresponding weights

```

```

207 theta_vec = linspace(0,pi/2,Ntheta);
208 weights=sin(theta_vec); weights=weights/sum(weights);
209
210 %preallocate results
211 t_theo = t_num(1:10:end);
212 sig_theo = zeros(1,numel(t_theo));
213
214 %loop over orientations, sum up results
215 for itheta = 1:Ntheta
216
217     theta=theta_vec(itheta);
218     B=3*sin(theta)*cos(theta)*T;
219     nu_pm = sqrt(B^2*a_eff^2/4+delta_nu_eff^2); %transfer frequency
220     transfer_amp = a_eff^2*B^2/(4*nu_pm^2); %amplitude of transfer
221
222     sig_theo = sig_theo+weights(itheta)*sign(a_eff)*proj*transfer_amp*...
223         sin(1/2*(2*pi*nu_pm)*t_theo).^2;
224 end
225 plot(t_theo,sig_theo,'o')
226
227 axis([xlim -0.1 0.8])
228 xlabel('t / \mu s')
229 ylabel('<I_z>')
230 legend('num.', 'theo.', 'location', 'northeast')

```

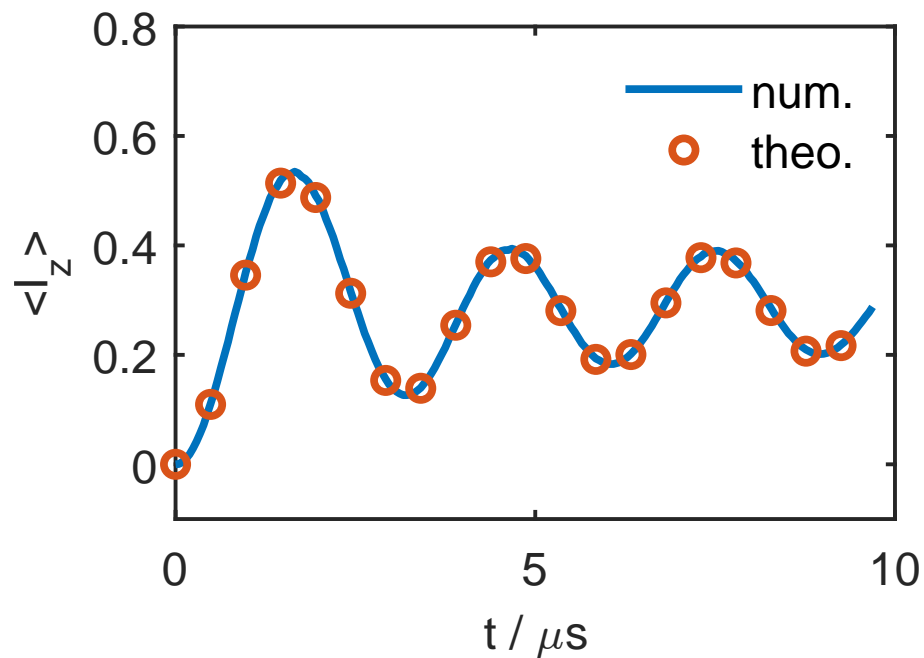


Fig. S4: Fully numerical simulation vs. effective Hamiltonian calculation.

S.2 Comparison of numerical and analytical computations for strongly coupled protons

Figure 4(b) in the main text showed a comparison of numerical and analytical computations for a proton at a distance of $r_{en} = 4.5 \text{ \AA}$. This is already quite close. Here we show what happens if one looks at protons that are even closer (2.5 \AA), see Figure S5. In this case, the hyperfine coupling is very strong. Nevertheless, the full first-order Hamiltonian (blue line) still perfectly describes the transfer. However, it is clear that only looking at the effective fields and the flip-flop terms (red) becomes more and more problematic for strong hyperfine couplings.

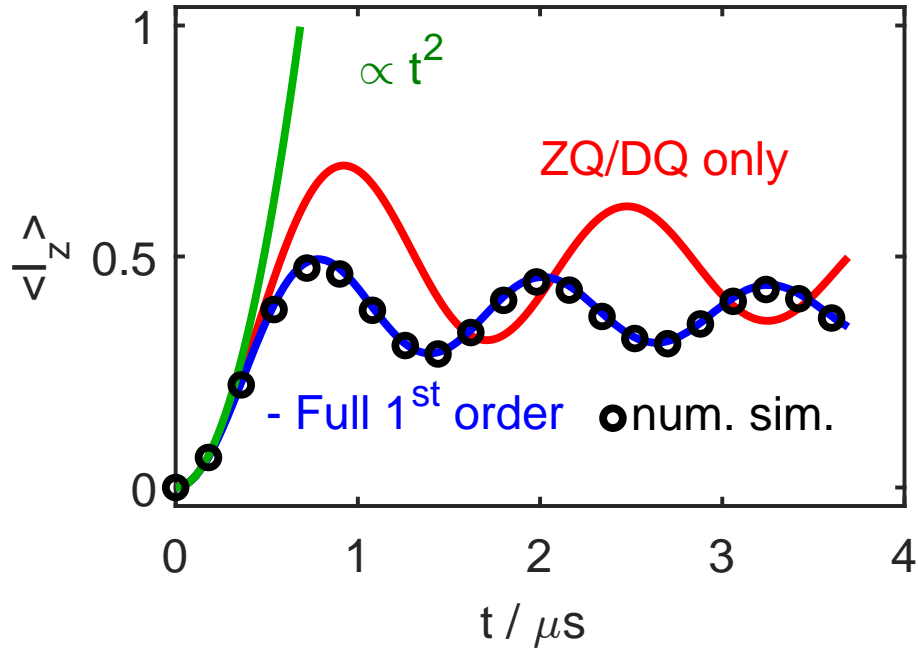


Fig. S5: Comparison of $S_z \rightarrow I_z$ polarization transfer efficiencies calculated using an effective Hamiltonian including all first order terms (blue) or only the flip-flop terms (red) with a full numerical simulation (black circles). A two-spin $e^{-1}\text{H}$ spin pair with a distance $r_{en} = 2.5 \text{ \AA}$ is used in the numerical simulations. This is a very strongly coupled proton. The green line illustrates the initial build-up

S.3 Three-spin transitions

Some small features in the Experimental DNP profiles cannot be explained by the electron-nuclear two-spin model. It is well known that there are also electron-nuclear-nuclear three-spin transitions. A comprehensive treatment for them would require second-order average Hamiltonian theory. However, the position of these features can be estimated by simply doubling the nuclear Zeeman frequency and then looking for matching conditions in exactly the same way as in the two-spin case. This is shown in Fig. S6.

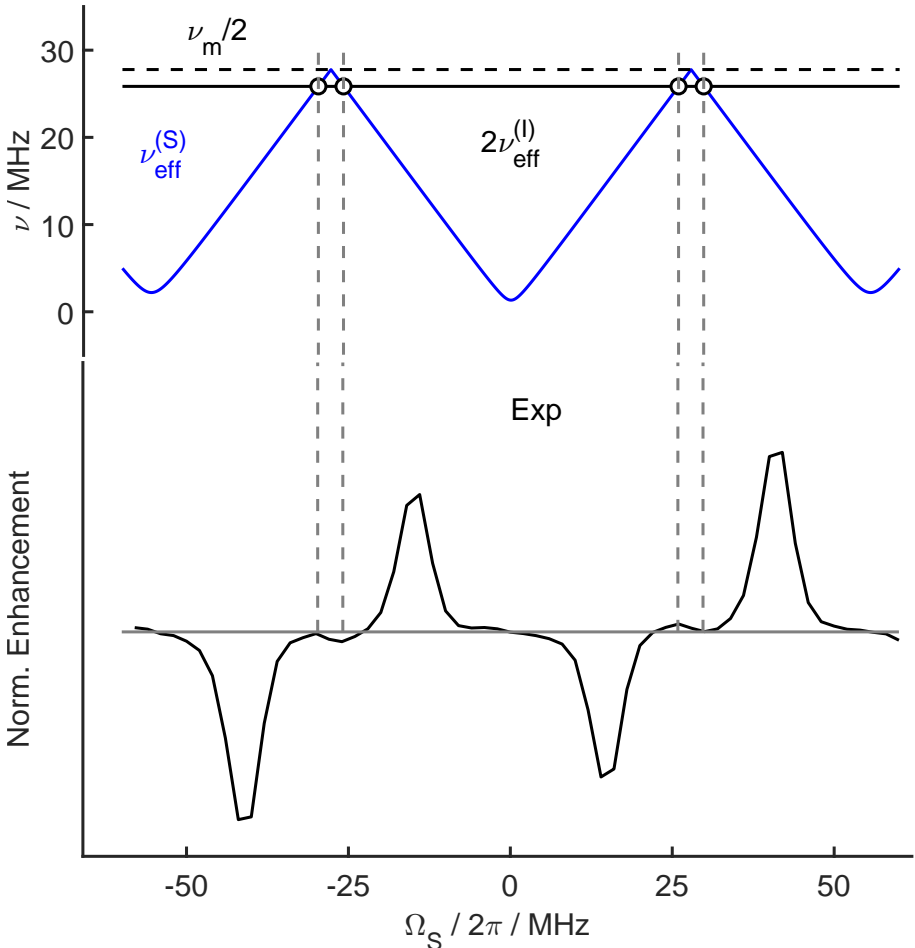


Fig. S6: Predicted offsets for three-spin transitions for XiX DNP with $t_{p,1}=12$ ns and $t_{p,2}=6$ ns.

S.4 Resonator profile

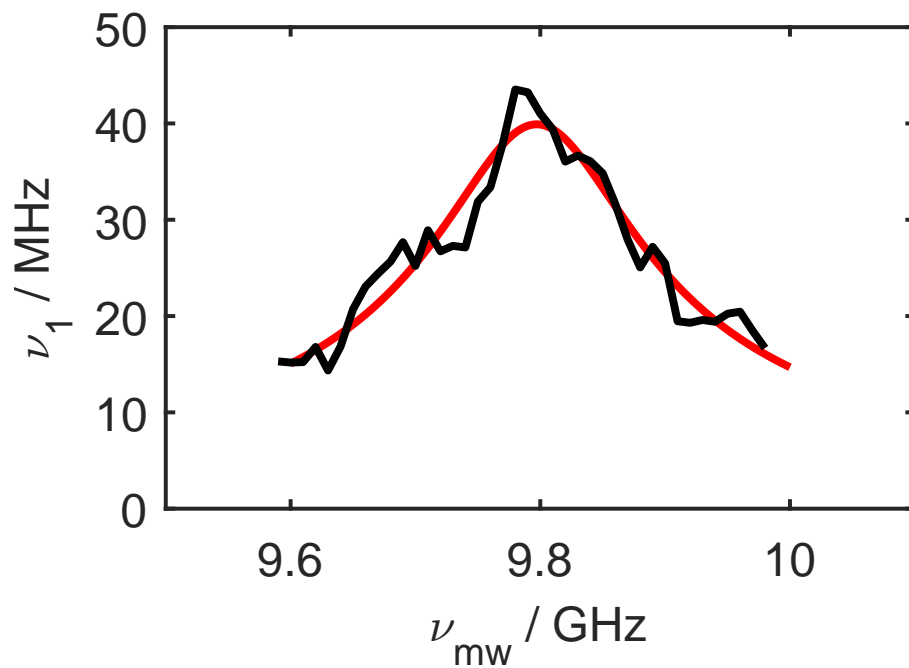


Fig. S7: Experimental resonator profile (black), determined by nutation experiments, and Lorentzian fit (red). $\nu_{1,\text{max}}=40$ MHz, $Q=61$.

S.5 Experimental data for the adiabatic solid effect (ASE)

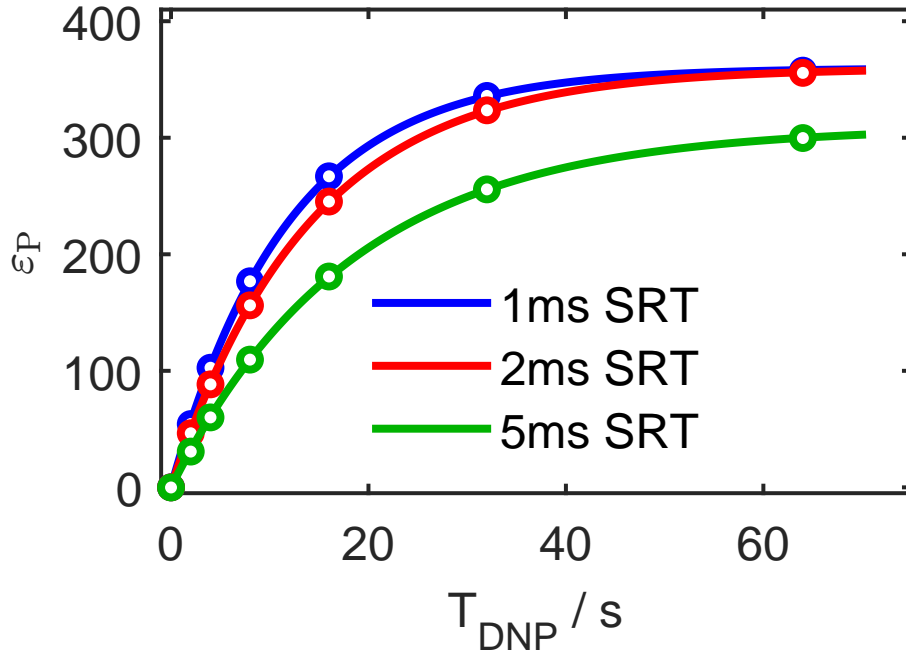


Fig. S8: Polarization build-up using the adiabatic solid effect with different repetition times.

Table 1: Enhancements ϵ_{max} , build-up times T_B , and sensitivity per unit time (i.e. signal per square root of time) $\epsilon_{\text{max}} \cdot \sqrt{T_{1,n}/T_B}$ for ASE. $T_{1,n} = 36.2 \text{ s}$. $T_{1,e} = 2.5 \text{ ms}$.

t_{rep}	ASE		
	1 ms	2 ms	5 ms
ϵ_{max}	360	360	309
T_B / s	11.9	14.1	18.3
$\epsilon_{\text{max}} \cdot \sqrt{\frac{T_{1,n}}{T_B}}$	629	578	435

S.6 Experimental determination of $T_{1,e}$

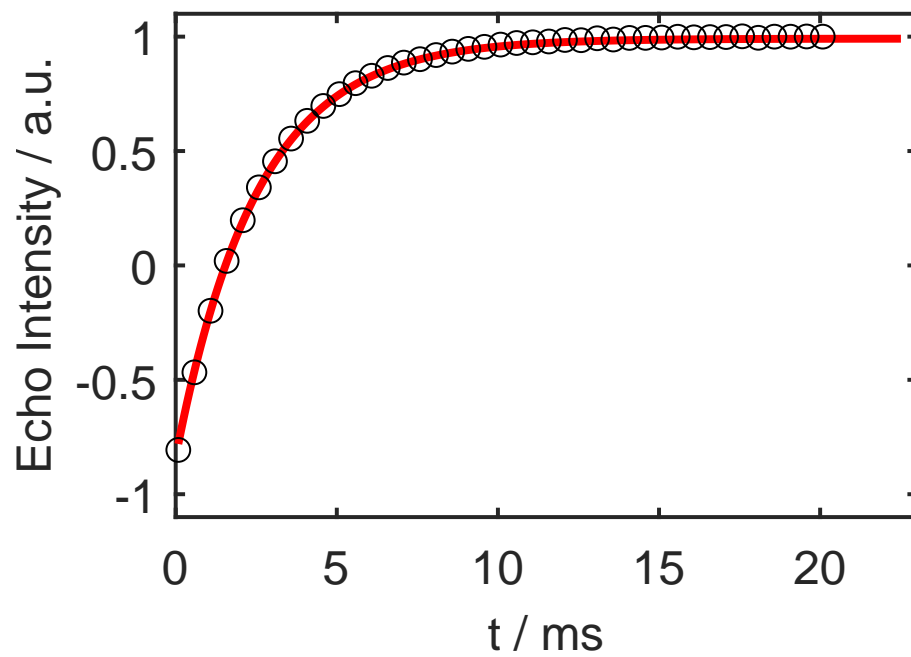


Fig. S9: Inversion recovery data for the electron spin (black circles) and exponential fit (red). $T_{1,e}=2.5$ ms

S.7 Experimental determination of $T_{1,n}$

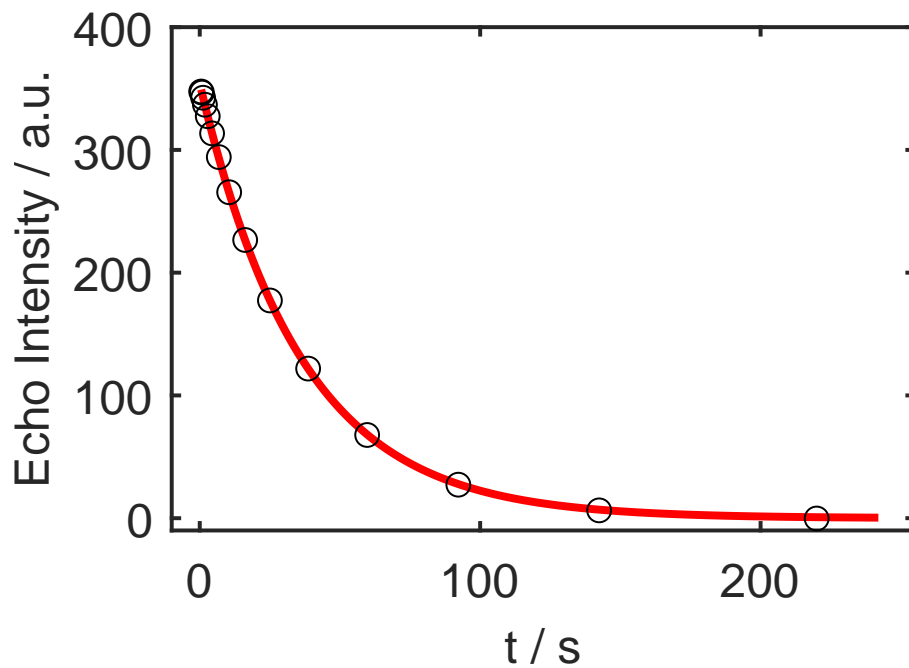


Fig. S10: Experimental proton polarization decay after 60 s of adiabatic solid effect DNP (black circles) and exponential fit (red). $T_{1,n}=36.2$ s

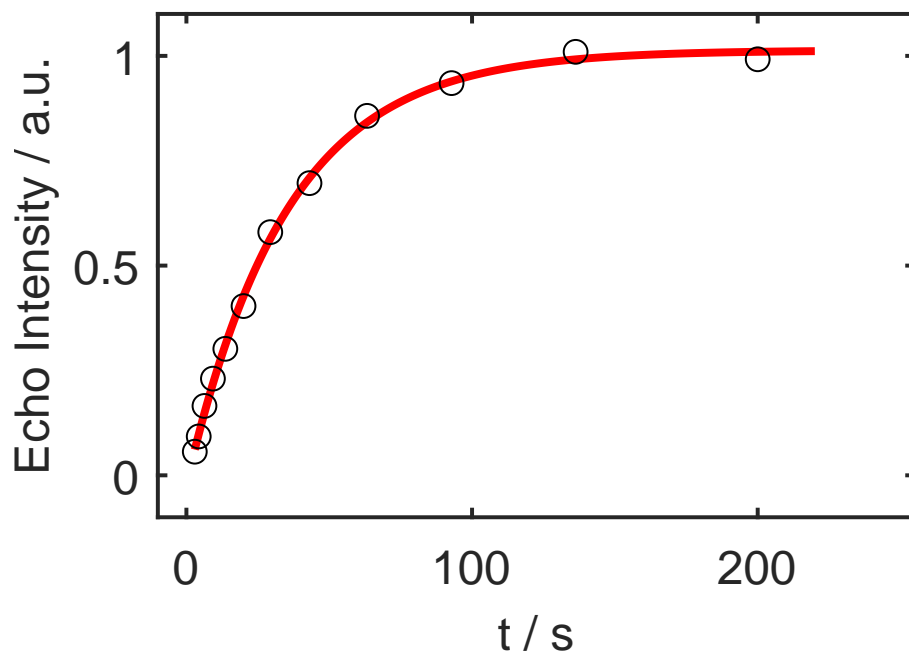


Fig. S11: Proton saturation recovery data without DNP (black circles) and exponential fit (red). $T_{1,n}=35$ s